Marine and Petroleum Geology 147 (2023) 105978

Contents lists available at ScienceDirect

Marine and Petroleum Geology

journal homepage: www.elsevier.com/locate/marpetgeo

Clay diagenesis and overpressure development in Upper Cretaceous and Tertiary shales of South Texas

B.S. Hart [a,*], J. Schieber [b], J. Kalinec [c]

[a] Department of Earth Sciences, University of Western Ontario, London, ON, N6B 5A7, Canada
[b] Indiana University Shale Research Lab, Indiana University, Bloomington, IN, 47405, USA
[c] kPa LLC, College Station, TX, 78745, USA

ARTICLE INFO

Keywords:
Pore pressure
Shale diagenesis
South Texas
Compaction

ABSTRACT

We studied the origins of overpressure, primarily using cuttings and wireline logs, in a nearly 4 km-thick succession of Tertiary and Upper Cretaceous shales and sandstones in the northwestern Onshore Gulf of Mexico. Our goals were: a) to specifically look for the microtextural changes in shale that are often inferred, by pore-pressure specialists, to develop in overpressured shale, and b) to test the utility of cuttings for that purpose. Overpressures begin approximately 2.5 km below the present ground surface and are moderate at the base of our study interval. Much of that section has velocity and density properties that are diagnostic of unloading, excess pore pressures generated after compaction has occurred. Our cuttings-based analyses included XRD and Rock-Eval measurements. Those datasets allowed us to define the changes in mineralogy and organic content (maturity and amount) with depth. We rule out organic maturation as a significant source of overpressure and instead identify clay diagenesis (smectite-to-illite transition) as the major source of excess pore pressure. Finally, we use SEM imaging of ion-milled samples to examine and document the nano-to micron-scale textural and mineralogic changes that occurred during diagenesis. Diagenetic quartz, present as overgrowths on quartz silt grains and microquartz intergrown with illite, is associated with the changes in clay mineralogy. Some nano-to micro-porosity can be preserved locally when detrital silt or rigid diagenetic minerals (mainly quartz and pyrite in our samples) prevent physical compaction. The stratigraphic offset between the onset of overpressure and the onset of clay diagenesis is probably due to the combined effects of the broad-scale stratigraphy (the section becomes sandier at shallower depths), and the temporal changes associated with overpressure generation and dissipation. Our experiment with cuttings demonstrated the utility and limitations of their use. Finally, our results challenge some of the assumptions about shale diagenesis that can be used during pore-pressure studies.

1. Introduction

Several mechanisms can generate overpressured shales, in which pore pressures exceed the hydrostatic pressure for a particular depth. Most of these processes are associated with some type of mechanical or chemical diagenesis of the shale that operates at the micro- or even nanoscale. Mechanical diagenesis is mostly associated with sediment compaction. Chemical diagenetic reactions include processes such as the conversion of smectite to illite, and maturation of organic matter to hydrocarbons. A summary of the mechanisms responsible for overpressure development was presented by Swarbrick and Osborne (1998).

The most common explanation for overpressure development in rapidly accumulating thick shale successions is compaction disequilibrium, in which shales accumulate faster than they can dewater. In this case, pore-filling fluids start to bear some of the weight of the overlying sediment column. At the grain level (micron-scale or smaller), compaction disequilibrium is thought to be associated with a slowing of mechanical compaction. As such, higher-than-expected porosity is preserved at depth. Porosity-dependent properties (velocity, density, resistivity) are also affected, and various analytical methods have been proposed for the estimation of overpressure from wireline log responses (e.g., Eaton, 1975; Bowers, 1995; Hart et al., 1995; Bowers and Katsube, 2002).

Secondary processes for overpressure development involve some type of fluid-pressure generation once sediments have compacted. Several mechanisms, including clay diagenesis, aquathermal expansion,

* Corresponding author.
E-mail address: bhart7@uwo.ca (B.S. Hart).

https://doi.org/10.1016/j.marpetgeo.2022.105978
Received 23 February 2022; Received in revised form 12 September 2022; Accepted 9 October 2022
Available online 19 October 2022

and hydrocarbon generation, can generate overpressures this way. Clay diagenetic processes affecting overpressure development include the conversion of smectite to illite, which releases water (and silica) thereby transferring some of the overburden stress onto the pore fluids if the latter are not free to escape (e.g., Lahann, 2002). Collectively these mechanisms have been termed "unloading" because they reduce the effective stress felt by the affected shales (Bowers, 1995). Wireline log responses are variably affected by unloading (e.g., Hermanrud, et al., 1998; Swarbrick, 2012; Zhang, 2011).

A common limitation of pore-pressure studies is that the micron-to nanoscale diagenetic processes are inferred, rather than documented via direct imaging. For example, Lahann and Swarbrick (2011) suggested that, in the absence of chemical diagenesis, the lowest porosity in shale will be controlled by irreducible pores associated with clay-bound water. The implication is that, without clay-bound water, shale porosity could conceivably be reduced to zero. Bowers and Katsube (2002) proposed several different pore-structure models (e.g., storage pores and connecting pores) based on mercury porosimetry but presented no direct imagery of those pore types. Avseth et al. (2010) focused on shale fabrics in which silt grains are supported in a clay matrix and proposed that shales are not normally cemented. These assumptions allowed Avseth et al. (2010), and references they cite, to develop various rock-physics models for pore-pressure prediction, velocity modeling, and other purposes. Conversely, SEM-based analyses of compacting shales provide information about diagenetic processes (e.g., Thyberg et al., 2010; Day-Stirrat et al., 2012) but are generally not linked to overpressure analyses.

One of the primary limitations on the integration of wireline-log-based rock-property analyses in overpressured shales and nano-to micro-scale observations of shale fabrics of is the general lack of intact samples through km-thick, structurally undeformed shale sections. The cost and logistics of taking whole cores at that scale is prohibitive. Intact, shale cores 100s of m long have been retrieved through scientific drilling (e.g., Day-Stirrat et al., 2012) but generally that drilling avoids overpressured sections. Sidewall cores from shales are available in some cases (e.g., Hart et al., 1995; Aplin et al., 2006) but are not regularly collected for analyses of shale diagenesis.

Here we present results from an investigation into the use of cuttings, collected from a shale-dominated section nearly 4 km thick, to relate grain- and pore-scale processes with wireline log-based pore-pressure analyses. Our specific goal was to integrate SEM imaging tools commonly used for studies of shale reservoirs (e.g., Loucks et al., 2012; Schieber et al., 2016), wireline logs, and other data to define diagenetic processes associated with overpressure development in Upper Cretaceous and Tertiary shales of the onshore Gulf of Mexico in South Texas. Our results provide important insights into relationships between shale diagenesis and overpressure development, but also illustrate the capabilities and limitations of the cuttings-based approach we used in our study.

2. Study area

Our porosity evaluation focuses on the Upper Cretaceous and Tertiary interval that overlies the Eagle Ford Formation in South Texas (Fig. 1). This 3–4 km thick, shale-dominated section was a passive margin during deposition and, other than some localized normal faulting, there is little structural deformation and no significant unconformities (i.e., gaps in geologic time) in the interval of interest.

Fig. 2 shows a simplified stratigraphic column for the interval of interest. Ages are based on Galloway (2008). Note the up-section transition from distal, calcareous shales and chalks immediately above the Eagle Ford (Austin Chalk, Anacacho) to the clastic-dominated uppermost Cretaceous and Tertiary section that includes the Wilcox Group, Queen City, and overlying sandy deposits. Locally, these sandstones can be reservoirs and/or aquifers, and drilling through them can be associated with various types of hazards (e.g., Bebout et al., 1982; Mace et al., 2000; Carpenter, 2015; Mitchell, 2017).

In a general way, the Upper Cretaceous section was deposited at the southern entrance to the Cretaceous Western Interior Seaway (KWIS). Pelagic limestones (including chalks) and marlstones of the Eagle Ford, Austin Chalk and Anacacho represent clastic-starved distal environments deposited at the southern extremity of that seaway. Marlstones of the Eagle Ford were organically enriched, allowing them to become prolific source rocks. Hydrocarbons retained in the Eagle Ford, and others that migrated into the overlying Austin Chalk, have been the primary drilling targets of the past decade in the current study area.

Galloway (2008) suggested the Navarro Group represents the first significant pulse of siliciclastic shales and sandstones derived from the nascent Laramide Orogeny to the west and southwest. The KWIS was still open at this time but closed by the end of the Cretaceous. The Early Paleocene Midway Shale represents a period of distal, mud deposition that is overlain by successive sequences of shoreline progradation and transgression along the Gulf of Mexico, leading to the outbuilding of the shoreline and shelf margin in that area. The Wilcox Group and Queen

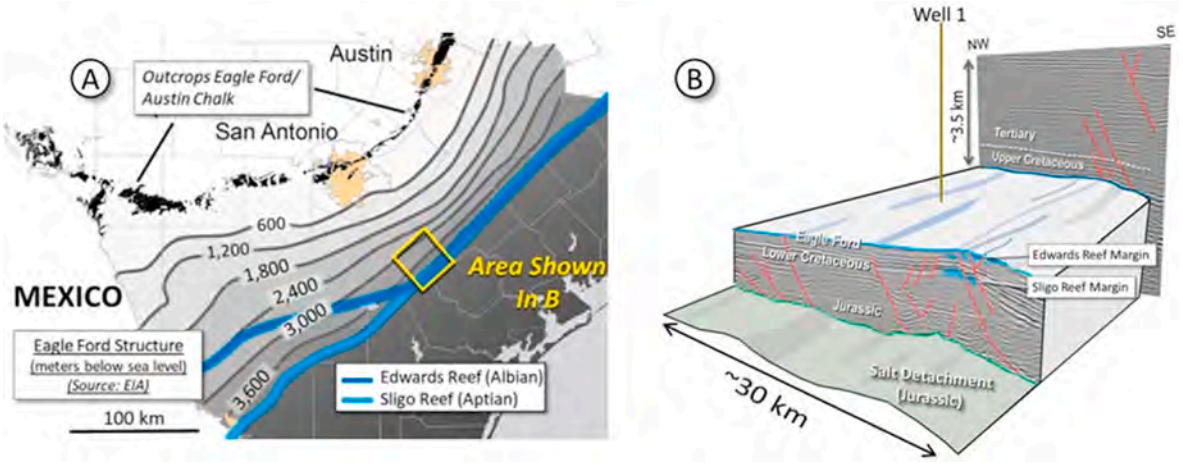

Fig. 1. A) Location map showing broad-scale structural contours. The Eagle Ford dips to the southeast upon the paleoshelf. Underlying Lower Cretaceous reefs (Edwards and Sligo) formed the shelf margin during Eagle Ford deposition. Yellow box shows the location of the 3D-seismic-based image shown in Part B. B) Annotated seismic imagery showing broad-scale structural configuration, ages of main stratigraphic units and approximate location of Well 1, the well for which cuttings data, borehole temperature, and LWD gamma-ray log were available for this paper. This paper focuses on the Upper Cretaceous and Tertiary section above the Eagle Ford. (For interpretation of the references to color in this figure legend, the reader is referred to the Web version of this article.)

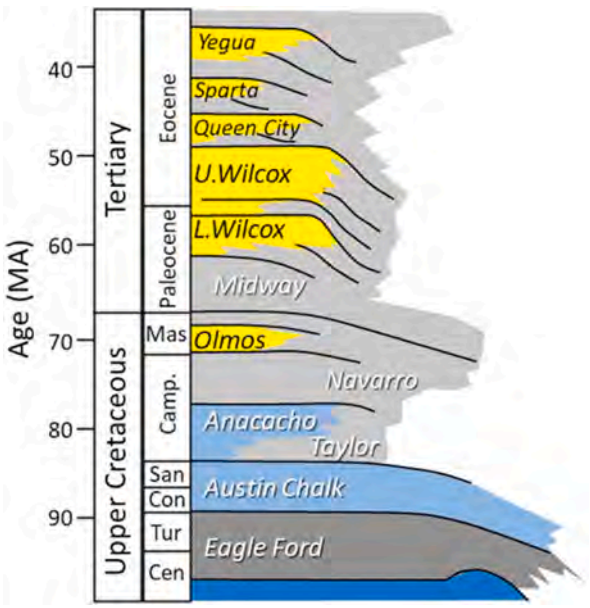

Fig. 2. Simplified stratigraphic column for the study area. Shale-dominated intervals shown in grey, carbonates in blue, and sandstones in yellow. Redrawn from Galloway (2008). (For interpretation of the references to color in this figure legend, the reader is referred to the Web version of this article.)

City Formation represent a significant pulse of sediment derived from uplift and erosion of the Rocky Mountain area during the Late Paleocene to Middle Eocene. Overlying shallow-marine sediments were derived from post-Laramide tectonic uplifts in that area (Cather et al., 2012).

Ground elevation at the well location is approximately 80 m above sea level. Xia et al. (2020) estimated approximately 300 m of uplift in our study area since the end of the Oligocene (23 Ma). The degree to which this relatively small amount of uplift would have affected the subsurface pressure or temperature profiles, or other properties of interest to our work, remains unknown and cannot be accurately modeled because some of the basic inputs to a basin model (e.g., crustal heat flow, permeability profile through the several km-thick section of interest) cannot be adequately constrained.

3. Database

Our principal database includes two distinct types of data. First, we analyzed cuttings samples from 29 different levels in a section ~3.9 km thick above the Austin Chalk. The cuttings were collected from the vertical section of an Eagle Ford development well (Well 1 in Figs. 1 and 3). The choice of which cuttings samples to analyze was based on examination of the gamma ray (GR) log collected while drilling, with samples being chosen from high GR (presumably clay-rich) intervals. For each of those samples, mineralogy (XRD) and organic contents (Rock-Eval) were analyzed by a commercial laboratory. The XRD analyses included assignment of clay minerals into relative fractions of smectite, illite/smectite, illite/mica/kaolinite, and chlorite, with the percentage of smectite in the illite/smectite category being given within a ± 5% range. The analyses provided us with grain-density data (calculated using mineral density values and mineral abundances) we subsequently used for porosity analyses. We did not attempt to make direct porosity or permeability measurements on the cuttings because we assumed that their integrity would be affected during the drilling, retrieval, and archiving process. Five samples were analyzed for vitrinite reflectance. In the text below, we supplement these data with mineralogy and rock-eval data from a core that penetrated the underlying Eagle Ford reservoir level. Full discussion of that latter dataset is beyond the scope of this paper.

Ten of the cuttings samples were analyzed by SEM. Samples were mounted on 1/2-inch diameter sample holders and ion milled over the entire exposed area. Unfortunately, because of random shapes of drill cuttings, it was not always possible to mill all cuttings perpendicular to bedding. Although we can use lamination or preferential grain orientation to infer how close to perpendicular a given chip was milled, it is not possible to assign the stratigraphically "up" direction. After milling, sample surfaces were examined without conductive coating with an FEI Quanta 400 FEG in low vacuum mode. Further details of the SEM imaging procedure are detailed in Schieber (2010, 2013).

The second data type consists of wireline logs. Unfortunately, we only had a gamma-ray log through this part of the section in Well 1. As such, we inferred resistivity, density, and p-wave velocity data from two nearby wells. We used these data to make stratigraphic picks, to define broad-scale lithology, and to calculate pore pressures. For Well 1 we also had a temperature log, measured while drilling (MWD) through the section above the Eagle Ford target.

4. Results

We begin this section by briefly describing the stratigraphy encountered in our wells. Next, we present evidence for overpressures in our study area. Finally, we use Rock-Eval, XRD, and SEM imagery to characterize the organic and inorganic diagenesis of the shale section of interest.

4.1. Stratigraphy

Fig. 3 shows the stratigraphy of the Upper Cretaceous and Tertiary section of interest, as defined by gamma-ray logs from three wells. The

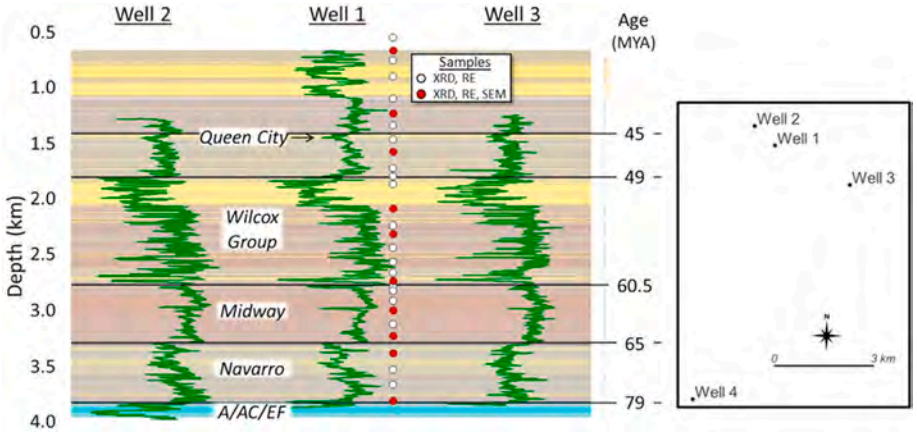

Fig. 3. Gamma-ray logs from three wells shown in map at right, displayed as a stratigraphic cross section datumed on the Queen City Sand (QC). Scales for all three logs range from 0 to 150 API units. Locations of cuttings samples from Well 1, and analyses performed on each, shown by dots. Note the lateral continuity of the stratigraphy between these wells. Depths shown at left are true vertical depth for Well 1, the primary focus of this paper. Color shading shows simplified lithology (yellow – sand, brown – shale, blue – carbonates). The Anacacho/Austin Chalk/Eagle Ford interval (A/AC/EF) is dominated by carbonates. Sequence-boundary ages from Galloway (2008). See text for further discussion. (For interpretation of the references to color in this figure legend, the reader is referred to the Web version of this article.)

interval between 1 km and nearly 4 km depth is dominated by shale, except for the Upper Wilcox Group that is sand-dominated and the Lower Wilcox Group that also is sandy. This ~3.8 km-thick siliciclastic section overlies the calcareous Anacacho, Austin Chalk, and Eagle Ford formations.

Note the lateral continuity of the stratigraphy between the three wells, located approximately 3.5 km apart. That continuity is important because the SEM, XRD, and Rock-Eval data presented herein are from Well 1 (the vertical portion of an Eagle Ford development well) but the density log we use subsequently is from Well 2 and the sonic log is from Well 3. As such, we are confident that the velocity and density measurements we use are representative of the rocks sampled by the cuttings.

4.2. Petrophysical analyses

We derived porosity from logs in two different ways. Issler's (1992) method was used to derive porosity from the p-wave sonic log in Well 3 (filtered to exclude intervals defined as sandstone):

$$\varnothing_{sonic} = 1 - ((\Delta t_{ma})/\Delta t)^{0.457}$$

where Δt is the sonic traveltime and the constants Δt_{ma} (matrix traveltime) and the exponent are those proposed by Issler for low-TOC, non-calcareous shales. The lithologic filtering was done using a Vshale ("volume of shale") curve derived from a depth de-trended GR log (to compensate for compaction effects on the GR response). A Vshale value of approximately .6 was found to be useful for distinguishing between intervals defined as "shale" on cuttings logs and those defined as predominantly sandstones or siltstones.

Density porosity ($\varnothing_{density}$) was calculated using:

$$\varnothing_{density} = (\rho_{ma} - \rho_b) / (\rho_{ma} - \rho_f)$$

Where ρ_{ma} is derived from a smoothed curve fit to grain-density values measured on the 29 cuttings samples from our well (locations in Fig. 3), $\rho_f = 1$ g/cc (fresh water) and ρ_b is the bulk density log from Well 2 filtered to exclude intervals defined as sandstone or clean siltstone.

The two porosity estimates are shown at left in Fig. 4. Note how the log-derived porosity estimates significantly diverge, with $\varnothing_{sonic} > \varnothing_{density}$, from approximately 2.5 to 3.3 km depth in the Lower Wilcox and Midway interval. This type of divergence is common in overpressured shales, where overpressures have developed in response to some type of unloading mechanism (e.g., Hermanrud et al., 1998; Tingay et al., 2009).

Fig. 5 plots velocity versus density for shales in our area. The Tertiary section above the Wilcox, the Upper and Middle Wilcox, and the Navarro Group all plot along a single trend that corresponds to normally compacting shales or shales in which compaction disequilibrium is the only pore-pressure generation mechanism. Shales from the Lower Wilcox and Midway fall distinctly below that line, in an area that indicates some type of unloading phenomenon (e.g., Bowers, 2001; Swarbrick, 2012; Dutta, 2016). This observation is consistent with the differences in porosity values calculated from the sonic and density logs (Fig. 4). Our sedimentation rate estimates (described next) and mineralogical analyses (Section 4.5) help us explain why the Navarro could have a different compaction history.

We used the porosity measurements and sequence boundary ages (Galloway, 2008) to estimate uncompacted sedimentation rates (mm/yr) for the main stratigraphic intervals using:

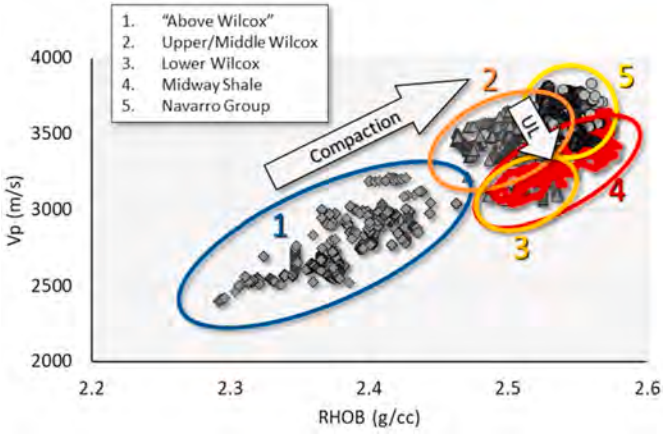

Fig. 5. P-wave velocity (Vp) versus density (RHOB) for Upper Cretaceous and Tertiary shales overlying the Eagle Ford/Austin Chalk reservoirs. Trends as defined by Swarbrick (2012). Trends from lower left to upper right correspond to normal or disequilibrium compaction trends with depth. The section above the Wilcox, the Upper Wilcox and the Navarro Group fall along this trend. Data from the Lower Wilcox Group and Midway Shale fall to the lower right of that trend, suggesting that some type of unloading mechanism (e.g., fluid expulsion associated with smectite-to-illite transition) has been operative in these intervals.

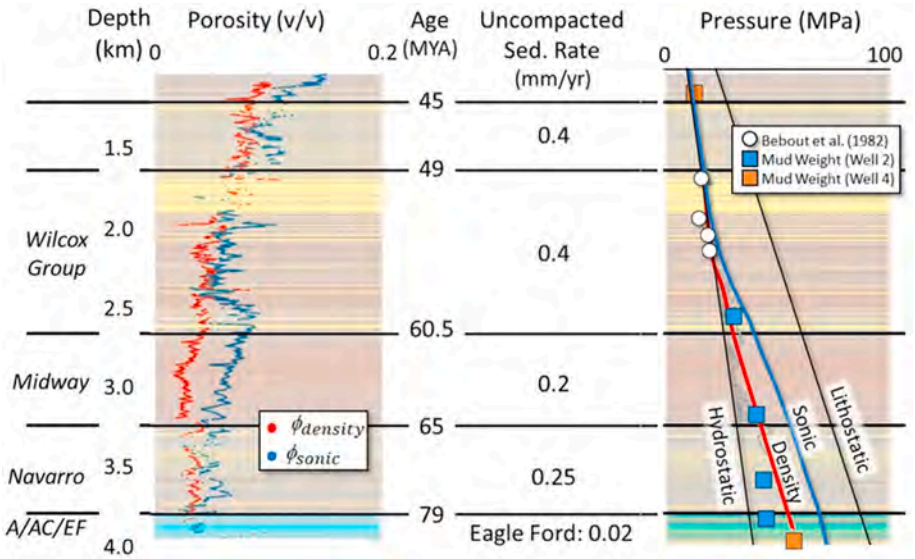

Fig. 4. Porosity and pore-pressure trends with depth. Porosity values (left) calculated from the density and sonic logs from Wells 2 and 3 respectively using methods described in the text. Porosity values from the density log were used, with sequence-boundary ages from Galloway (2008) to calculate uncompacted sedimentation rates (center). Smoothed pore-pressure estimates from the density log of Well 2 and the sonic log of Well 3 shown by the red and blue curves respectively. Grey curve shows pore-pressure estimated using the method of Hart et al. (1995). It suggests more variability in the pore-pressure profile than the density-derived curve (red) but similar trends. White dots are pressure measurements from Upper Wilcox sandstones in nearby wells. Blue and orange squares are pressures calculated from mud weights for Well 2 and Well 4 respectively. Depth shown is true vertical depth. See text for further details. (For interpretation of the references to color in this figure legend, the reader is referred to the Web version of this article.)

$$\text{Uncompacted Sedimentation Rate} = Z \,/\, \Delta A \times \left(1 - \varnothing_{avg}\right) / \left(1 - \varnothing_{o}\right)$$

Where Z is the thickness between two sequence boundaries, ΔA is the difference in age between those two dated stratigraphic boundaries (Fig. 4), $\varnothing_{avg}$ is the average $\varnothing_{\text{density}}$ in the interval and $\varnothing_o$ is an estimate of the average starting porosity (63%) derived by fitting an exponential curve to density porosity above 2 km depth and assuming the original ground surface would have been 300 m above current sea level. Given the potential error bars associated with all those values, we view the calculated uncompacted sedimentation rates values as order-of-magnitude estimates. Nevertheless, the numbers suggest a doubling in sedimentation rate from the Navarro and Midway intervals into the Wilcox to Queen City intervals. Sedimentation rates for these siliciclastic-dominated intervals are an order-of-magnitude higher than those calculated for the calcareous/marly Eagle Ford in this area, using age constraints for that unit provided by Denne et al. (2016).

Swarbrick (2012) suggested that sedimentation rates could be used to define a "fluid retention depth", a burial depth at which overpressures should start developing for different shale lithologies. Using sedimentation rates presented in Fig. 4 and assuming a silty shale composition, overpressures in the Midway section should have developed once that interval had been buried to approximately 0.8–1.2 km depth.

4.3. Pore-pressure estimation

We estimated pore-pressure two ways, using density- and sonic-log data from Wells 2 and 3 respectively (Fig. 4). We first used the method of Hart et al. (1995) that relates porosity, effective stress, and pore pressure. We also used sonic-log data from Well 3 and an adaptation of Bowers' (1995) method that relates velocity, effective stress, and pore pressure. Vertical stress was estimated by integrating the density log from Well 2 over the ~4 km section of interest. This stress-estimation method accounts for changes in lithology in the section, where present. Other details of the calculations are not presented here, for brevity, but are available from the authors upon request. These and similar methods have proven themselves effective for pore-pressure prediction in young, rapidly deposited, shale-dominated successions (e.g., Bowers, 2001; Swarbrick, 2012) like those in our section of interest.

The red and blue pore-pressure curves presented in Fig. 4 are a manually smoothed interpretation of the density- and velocity-based results. We choose to present a smoothed curve because the log-based methods can suggest an unrealistically wide variability in pore pressure over a short depth, as seen by comparing the grey and red curves in the plot. Unfortunately, direct pore pressure measurements are not available from the section of interest for any of the wells we used. As such, we show pressure measurements from the Upper Wilcox presented by Bebout et al. (1982) and pore-pressures calculated from mud weights for Well 2 and Well 4 (Fig. 3). We chose not to calibrate the curve to measured pore pressures in the calcareous Eagle Ford Shale because: a) it has a very dissimilar mineralogy to the overlying Tertiary shales (next section) and so compaction trends would not be similar, and b) a parallel study indicated that overpressures in the Eagle Ford are mostly related to hydrocarbon maturation (Kalinec and Hart, 2021).

Together, these data and our analyses suggest that pore pressures in Middle Wilcox shales are hydrostatic from the surface down and that overpressures in the Lower Wilcox begin at approximately 2.5 km depth, That depth approximately corresponds to the level at which the density- and sonic-log based porosity estimates diverge (Fig. 4) and to the top of the Lower Wilcox/Midway interval in which velocity and density data suggest the effects of unloading (Fig. 5). Of note is that the pressure curve derived from the density log (red) will underestimate pore pressure if a secondary pore-pressure generation mechanism (unloading) was active (Hart et al., 1995).

As noted by Morris et al. (2015), drillers select mud weights based on their expectations of pore pressures Therefore, in the absence of actual pore-pressure measurements in the ~1.2 km-thick section between the Lower Wilcox and the top of the Anacacho Formation, and lacking knowledge of drilling engineers' criteria for planning mud weights in Wells 2 and 4, we interpret the actual pore pressures to be intermediate between the red and blue curves on Fig. 4.

4.4. Organic matter and temperature data

Overpressures and porosity can be associated with organic maturation and hydrocarbon generation. As such, we sought to characterize the type and maturity of organic matter in the section overlying the Eagle Ford and Austin Chalk. The TOC data shown in Fig. 6 indicate that most of the section above the reservoir level contains low (≤1%) TOC values, except for an interval within the Midway Shale where values approach 2%. All these values are much lower than those observed in Eagle Ford marlstones at the base of the section.

Rock-eval data help constrain the nature of the organic matter. The HI vs T_{max} plot in Fig. 6 shows organic matter in the Upper Cretaceous to Tertiary overburden section to be Type III-IV, gas-prone to inert kerogen with little or no potential to generate liquid hydrocarbons even though they are, from a maturation perspective, in the oil window.

The vitrinite reflectance measurements, combined with measurement-while-drilling (MWD) temperatures, provide data that can be used to constrain organic and inorganic diagenetic reactions (see Discussion). Fig. 6 shows the MWD temperature profile from the section above the Eagle Ford. We interpret three distinct segments to the profile: the section from the surface to the Upper Wilcox has a gradient of 27.3 °C/km, the middle part of the Wilcox is approximately isothermal, and the interval from the Lower Wilcox to the Eagle Ford has a gradient of 47.4 °C/km. The type of segmented temperature profile seen in Well 1 is observed in other parts of the onshore and offshore Gulf of Mexico along the Texas coast (e.g., Bodner and Sharp, 1988; Nagihara and Smith, 2008).

Although there is no standard method for calibrating MWD temperature data to in situ values, we suggest those data are good estimates of in situ values because: A) The MWD measurements match bottom-hole temperatures from wells that produce from the Wilcox Group (Fig. 6A). B) Extrapolation of the lower gradient to the reservoir (Eagle Ford) level predicts a temperature that agrees very well with corrected bottom-hole temperature from a well test there. C) The observed gradients and absolute temperatures are consistent and nearly identical to those observed by Bebout et al. (1982) in DeWitt County, immediately to the northeast of our study area.

Fig. 6 also shows measured vitrinite reflectance values (from cuttings) and values estimated from T_{max} values determined from Rock-Eval measurements on cuttings samples. Like the MWD temperature data, it is possible to identify (visually) three segments to the profile. Together, the published observations of segmented temperature profiles elsewhere in the greater Gulf of Mexico basin, the agreement between our gradients and published values in our study area, and the similarity between MWD logging temperatures and Ro values leads us to conclude that the segmented temperature profile from MWD logging is real and not some type of artifact from drilling operations.

4.5. Mineralogy

Fig. 7 summarizes the bulk mineralogy of the shales in a ternary diagram, and Fig. 8 shows all the XRD data in profile format. Three distinct zones are apparent. The upper part of the section (surface to base of the Midway) is siliciclastic, generally with little/no calcite. Zeolites, common components of the Oligocene and Miocene section in the Gulf Coast are present in the uppermost two samples. Some samples, above the Wilcox Group, can have up to ~9% calcite as foram tests and cements in sandstone or siltstone fragments included in the cuttings. Small amounts of siderite are present as cements in some of the samples. Clay content exceeds 50% in the siliciclastic-dominated portion of the section, particularly in the Midway Shale. Samples from the Austin

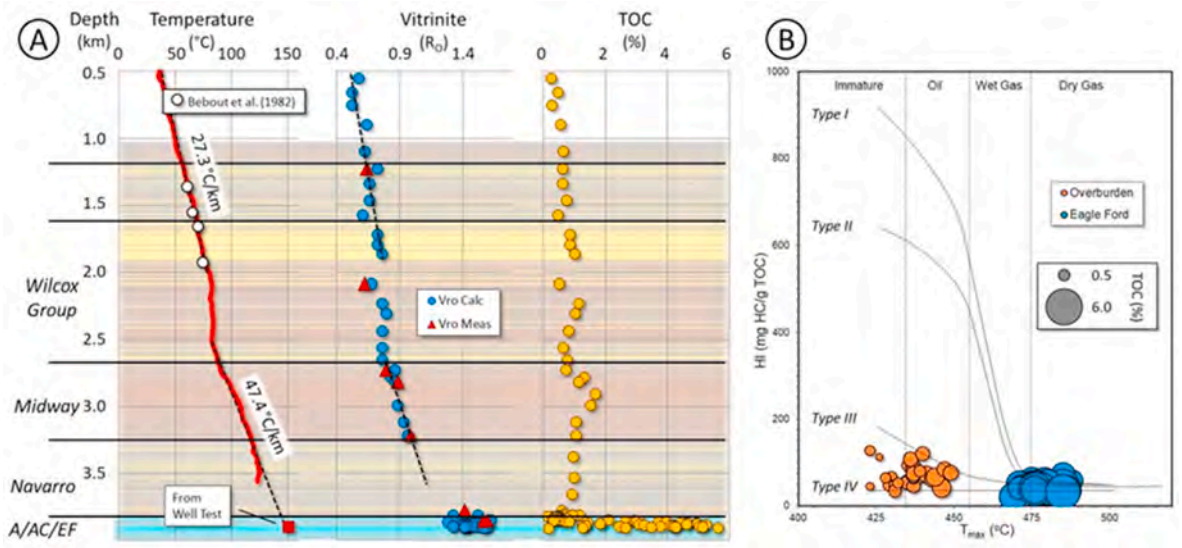

Fig. 6. A) Profiles of (left to right): i) Temperature (red) from measurement-while-drilling supplemented by bottom-hole data from Bebout et al. (1982) and bottom-hole temperature from a well test, ii) Vitrinite reflectance (measured and calculated from T_{max}), iii) TOC. B) Hydrogen index (HI) vs T_{max} data from the study well, data-point size scaled to TOC. Note the contrast between the gas-window, high-TOC Eagle Ford samples and the low-TOC samples from the overburden interval. Other data, from thermally immature samples, indicates the Eagle Ford organic matter originated as Type I or Type II kerogen (i.e., was oil prone; e.g., Hart et al., 2020). The low-TOC organic matter from the overburden section appears as Type III to Type IV kerogen, having little to no capacity to generate oil, and is not thermally mature enough for any oil it may have generated to have thermally cracked to gas. Depth shown is true vertical depth. (For interpretation of the references to color in this figure legend, the reader is referred to the Web version of this article.)

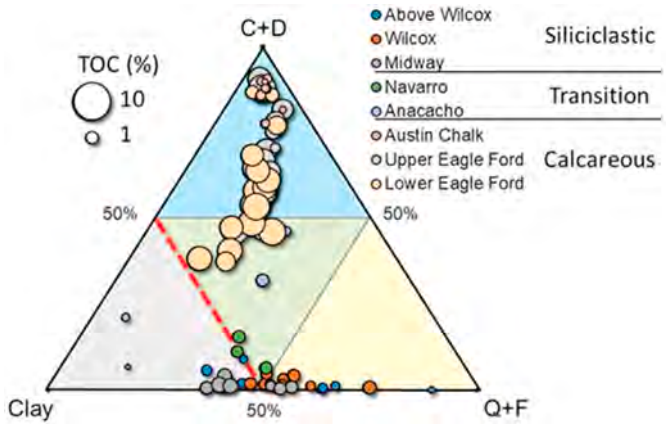

Fig. 7. Ternary diagram comparing mineralogy of shales in the principal stratigraphic units. Data-point size is proportional to the TOC (scale in upper left). Low-TOC, low-calcite siliciclastic shales extend down to the base of the Midway. The calcite content of the Navarro and Anacacho shales is somewhat higher, but the TOC is still low. The Austin Chalk is mostly composed of low-TOC limestones. The Eagle Ford is dominated by high-TOC, calcareous shales (marlstones). Note that sample density in the Eagle Ford and Austin Chalk is much higher (~30 cm spacing) than in the overlying section. Labeling includes C + D for calcite + dolomite and Q + F for quartz + feldspar.

Chalk and Eagle Ford formations are calcareous (marlstones and limestones), but the Eagle Ford samples have high TOC (typically 6–8%) and the Austin Chalk samples typically have <2% TOC. Shales in the Navarro Group and Anacacho Formation are transitional, in that they generally have >10% calcite content. This compositional difference may help to explain why the density/velocity relationship of the Navarro appears to be different from that of the overlying shales (Fig. 5).

Clay-fraction mineralogy is shown on the right in Fig. 8. Smectite was reported in the uppermost three samples but is absent in the underlying section. Instead, XRD analyses show the presence of mixed-layer illite-smectite (I/S) with the proportion of smectite interlayers decreasing with depth and the amount of illite interlayers increasing with depth. The relative amounts of illite/mica (I/M), kaolinite and chlorite also increase downward, to approximately 3.5 km, into the Navarro Group. Below that, the amounts of I/M and kaolinite decrease and I/S increases.

Fig. 9 illustrates relationships between different types of clay minerals as well as potassium feldspar. Colors and data-point size both indicate sample depth. The amount of potassium feldspar is positively correlated to the amount of smectite in I/S, and both quantities decrease with depth (Fig. 9A). Chlorite is negatively correlated with the amount of smectite in I/S, with chlorite content increasing with depth (Fig. 9B). Chlorite and I/M are positively correlated, both increasing with depth, down to the base of the Wilcox Group. Below the Wilcox, the I/M content decreases whereas the chlorite content remains constant (Fig. 9C). A similar trend is present when chlorite is plotted against kaolinite (Fig. 9D). Both increase with depth to the base of the Wilcox Group, after which kaolinite decreases, and chlorite remains constant. These trends are broadly consistent with expected chemical diagenetic reactions for clays (Boles and Franks, 1979; Worden and Morad, 2003). However, chlorite does not continuously increase with depth, and we speculate that a lack of iron in the Midway and Navarro shales, perhaps related to their distal depositional setting, may have been a limiting factor.

We plot illite in I/S as a function of temperature in Fig. 10 and compare our data to other datasets from the Gulf of Mexico. Shown this way, we interpret our data to show the smectite-illite conversion process to have proceeded in a way that is typical for the region. Conversion is underway by 60° and continues to over 100°. Our data show that not all smectite is converted to illite in the mixed-layer clays even at temperatures beyond ~110°, in the Midway Shale (Fig. 6). Mineralogy data presented in Fig. 8, showing an absence of potassium feldspar below the Wilcox Group and increase in calcite content, lead us to suggest that the illite content of mixed-layer smectite-illite plateaus at ~75% because the more distal depositional setting of the Midway and Navarro Group shales led them to be relatively impoverished in potassium feldspar.

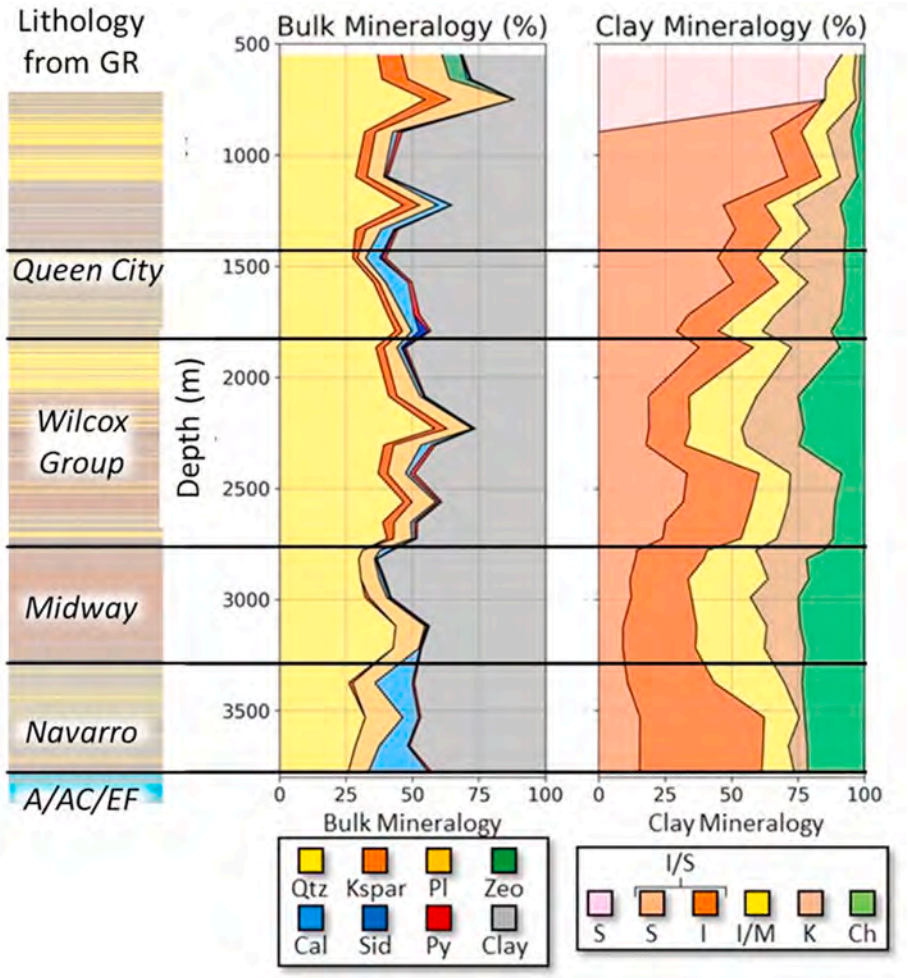

Fig. 8. Data from Well 1. Lithology (left track) is derived from the gamma-ray log. A clastic color coding (yellow – sand, brown – shale) is used for the section down to the base of the Navarro. A carbonate shading (blue – limestone, brown – shale) is used for the Anacacho/Austin Chalk/Eagle ford (A/AC/EF) interval. Second track from left shows bulk mineralogy of cuttings in the overburden section for Austin Chalk/Eagle Ford wells. Samples were selected for analyses based on the gamma-ray log character. Track at right shows clay mineralogy. Color coding for mineralogy: Q – quartz, Z – zeolites, Ksp – potassium feldspar, P – plagioclase feldspar, C – calcite, Si – siderite, Fe – iron sulfides (pyrite and marcasite), Cl – clays. Track at right shows clay mineralogy for the same cuttings samples. S – smectite, I/S – mixed-layer smectite-illite divided into smectite (S) and illite (I) components, I/M – illite/mica, K – kaolinite, Ch – chlorite. Depth shown is true vertical depth. (For interpretation of the references to color in this figure legend, the reader is referred to the Web version of this article.)

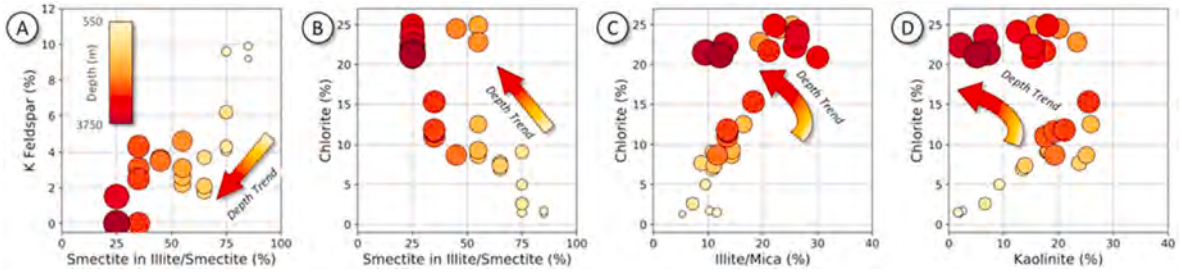

Fig. 9. (A) Potassium feldspar (total weight percent) versus the proportion of smectite in illite/smectite (as percentage of the clay fraction). (B) Chlorite versus the proportion of smectite in illite/smectite (both as percentage of the clay fraction). (C) Chlorite versus illite/mica (both as percentage of the clay fraction). (D) Chlorite versus kaolinite (both as percentage of the clay fraction). Bubble size and color are both scaled to depth in each graph. See text for further discussion. (For interpretation of the references to color in this figure legend, the reader is referred to the Web version of this article.)

4.6. SEM imagery

For each sample of cuttings, we began our SEM imaging at low magnification to assess the range of lithologic variability captured by the XRD analyses. Fig. 11 shows selected examples. The pie charts in the upper right illustrate the bulk mineralogy for the cuttings samples. Because the cuttings were randomly oriented on the SEM mount, the overview allowed us to estimate the approximate orientation of stratification for some of the samples. Finally, the shape of the cuttings at low magnification provided qualitative information about the existence of overpressure at the sample depth. Splintery and/or angular shale cuttings are usually associated with overpressured intervals or transitions from normally pressured to overpressured parts of the section (Fertl, 1976; Beaumont and Fiedler, 1999).

As seen in Figs. 11 and 12, and despite our efforts to select cuttings from shale-dominated intervals, the cuttings samples include shale, siltstone, and sandstone. This type of mixture, especially in the Wilcox Group interval, arises because of the interbedded character of those strata (e.g., Olariu and Zeng, 2018; Landry et al., 2020a), even in parts of the section that are defined as shales based on gamma-ray log cutoff values. Log resolution is simply inadequate to identify the mm-to cm-scale lithologic heterogeneity that is present in the section. As such, the XRD analyses need to be understood as representing the mineralogic composition of a variety of lithologies, not just shale.

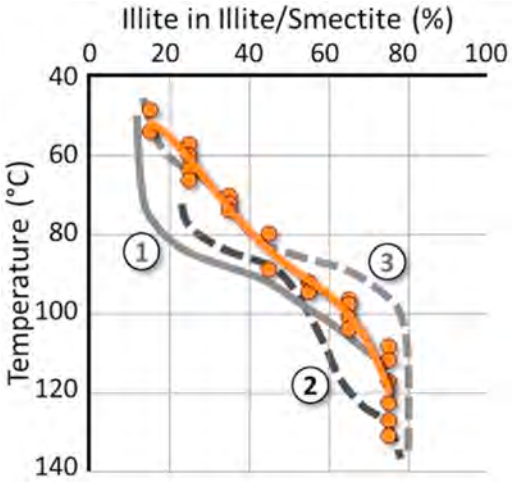

Fig. 10. Changes in illite content of illite/smectite as a function of present-day temperature in our well (orange dots and orange trendline) compared to trendlines from other parts of the US Gulf Coast (1. Jennings and Thompson, 1986; 2. Perry and Hower, 1972; 3. Hower et al., 1976). (For interpretation of the references to color in this figure legend, the reader is referred to the Web version of this article.)

The presence of sandstone cuttings in our SEM is useful for at least two reasons (Fig. 12). First, the presence of concavo-convex and planar grain contacts indicates the sandstones have been buried deeply enough to undergo some pressure solution. These types of contacts are visible in sandstones below ~1200 m present-day depth. The broad constraints on burial history presented in Section 2 suggest that these samples may have been buried beyond 2 km depth in the Eocene. That type of compaction suggests, in a qualitative way, that physical compaction of clay-dominated intervals would have been likely for shale cuttings from the same depths. Second, the sandstone images show that some clays defined by XRD are the product of diagenetic alteration of other minerals, most plausibly feldspars. As such, it is important to recognize that clay mineralogy trends defined by XRD (e.g., Fig. 8) are influenced to a greater or lesser degree by diagenesis of sandstone/siltstone cuttings samples included in our analyses. We note that the vertical resolution of wireline logs (gamma ray, density, sonic, etc.) is not sufficient to define mm-to cm-scale interbeds of shale, siltstone, and sandstone that are likely to be present in our section (e.g., Aplin and Macquaker, 2011; Hart et al., 2013; Landry et al., 2020a, 2020b) and so we deliberately analyzed the bulk properties of the "shale intervals" (defined petrophysically).

The SEM images show the presence of authigenic quartz cement in shales beginning at ~1500 m present-day burial depth (Fig. 13). That cement occurs in two different forms. Quartz overgrowths on detrital quartz grains are angular to euhedral and grain-rimming. They can be up to several 100 nm thick on silt-size detrital quartz grains. Microquartz (*sensu* Thyberg et al., 2010) is also present in clay-rich to clay-dominated shales, where the microquartz appears to be physically intergrown with adjacent clays and, at times, physically attached to them (Fig. 14). Relict quartz overgrowths, formed during a previous cycle of burial diagenesis, are observed in the shallowest sample (Fig. 13A). This abraded form to the overgrowths indicates that they did not form following Tertiary deposition and burial.

Because the cuttings could not be milled exactly perpendicular to stratification, we did not attempt to quantify clay mineral anisotropy from our imagery. However, qualitative observations of the SEM imagery indicate a progressive increase in grain alignment, decrease in porosity, and increased crystallinity with depth (Fig. 15). The shallowest sample, having ~80% of the clay minerals as smectite, provided no useful information about grain alignment at that depth. Those cuttings consisted of semi-consolidated mud, with randomly oriented clays, which dried during SEM preparation and imaging (Figs. 11A and 15A). By ~1200 m the predominantly mixed-layer clays show a distinct physical alignment, whereas by 2000 m the illite-rich I/S and I/M are well aligned and tightly packed, although microquartz crystals, detrital quartz silt and other larger crystals hinder clay alignment when those rigid grains are present (Fig. 15E). The heterolithic mix of siliciclastic and biogenic materials observed in the Navarro Group samples appears to have hindered compaction-induced grain alignment (Fig. 15F), at least compared to clay-dominated fabrics present in other samples. It is quite likely that these shales are bioturbated (lacking primary laminations), but intact core would be needed for verification. Unfortunately, there are no published descriptions of Navarro Group sedimentology for our study area.

A parallel study of high-resolution SEM mosaics of cuttings from the same well (Landry et al., 2020a, b) highlighted some of the challenges faced when attempting to quantify porosity from SEM imagery of cuttings samples. Among those challenges is defining a representative elementary area for image analysis in highly heterogeneous materials like shales. That study defined an irreducible porosity of 4–5% in clay-rich lithologies (not including micro-cracks of indeterminate origin), but nano-scale pores can be preserved in areas where larger rigid grains prevented compaction (Schieber, 2010). Similar relationships are seen in our imagery (Fig. 16).

Our SEM images show the presence of slot-shaped pores that are referred to as microcracks (μc; Figs. 13, 14 and 17). The cracks are present around the margins of silt grains, between clay platelets, and whenever approximate orientations are definable, approximately parallel to bedding (Fig. 17). None of the microcracks we observe show signs of mineralization within the crack. We contend that most such pores seen in our images are artifacts formed by pressure release as the shale cuttings are brought to the surface, and that they are not open in the subsurface. The rounded to platy shape of the cuttings permits stress release (expansion) in directions other than parallel to bedding. However, in some cases, convincing arguments can be made that individual microcracks may be primary, for example if the clays were sheltered from physical compaction by neighboring larger, rigid grains.

5. Discussion

We organize our discussion into three themes. First, we examine the evidence for overpressure in the section of interest and discuss possible causal mechanisms. Next, we compare the microfabrics observed in SEM images to some of the conceptual models used by geophysicists. Finally, we examine the advantages and limitations of using cuttings for the work we undertook.

Like Gordon and Flemings (1998), who studied a somewhat similar but younger (Plio-Pleistocene) section in the offshore Gulf of Mexico, we contend that the stratigraphic and structural history of our study area is the fundamental control on overpressures in our area. The broad-scale stratigraphy studied by those authors consisted of distal shales >1 km thick, overlain by a >2 km-thick section of deltaic and fluvial sands and shales. Their numerical modeling and data indicated that excess pore pressures, if developed, would more readily dissipate in the sandy sections (like the Wilcox and overlying units in our area) but would be more readily preserved in low-permeability shale sections (like the Midway and Navarro of our area).

The analyses of Gordon and Flemings (1998) also highlight the importance of understanding the distribution of overpressure as a dynamic system. Excess pore pressures have evolved (grown, dissipated) through time. Our study area may have been uplifted as much as 300 m since the Eocene. As such, the observed relationships between the onset of overpressure and depth, or temperature, or petrographic evidence for clay diagenesis in our area may not be truly indicative of the relationship between cause and effect. We keep those caveats in mind during the following discussion.

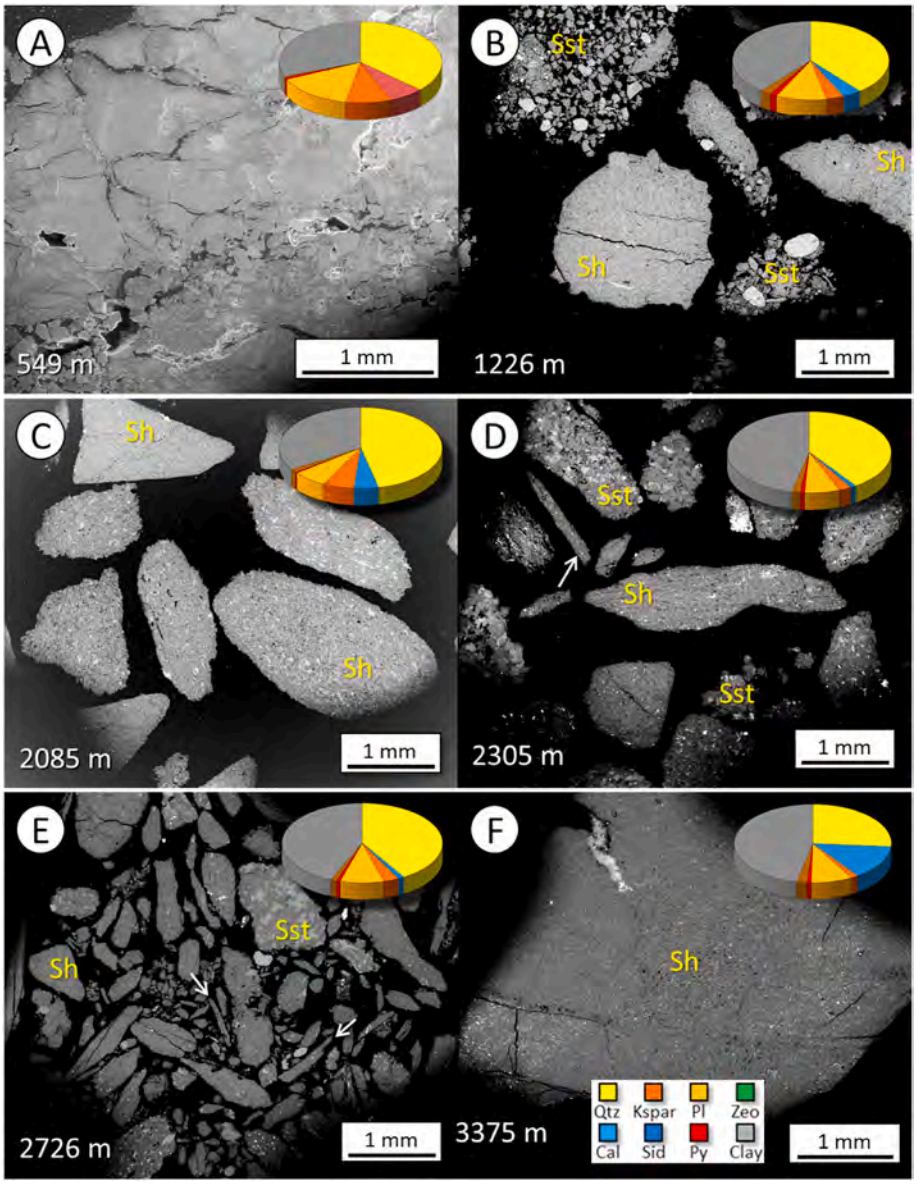

Fig. 11. Selected low-magnification SEM images of cuttings samples (all in backscatter electron mode). Nominal depth of each sample shown at lower left. Pie chart in upper right shows mineralogy defined by XRD (color code shown at lower right). A) 1226 m. Cuttings in this image include shale (Sh) and sandstone (Sst). Cracks in circular shale sample in middle suggest approximate orientation of stratification B) 2085 m. All samples in this image are shale (Sh). C) 2305 m. Cuttings in this image include shale (Sh) and sandstone (Sst). Note presence of splinter-shaped shale fragment (white arrow). D) 2726 m. Cuttings in this image include shale (Sh) and sandstone (Sst). Note presence of splinter-shaped shale fragments (white arrows). The long axes of the splinter-shaped cuttings are approximately parallel to bedding. The orientations of most cuttings, relative to bedding, cannot be defined (samples milled oblique to bedding). (For interpretation of the references to color in this figure legend, the reader is referred to the Web version of this article.)

5.1. Overpressure: magnitude and causes

As a first question, it might be reasonable to ask whether overpressures are indeed present in the Upper Cretaceous and Tertiary shales we examined. Although we do not have any direct pressure measurements in the shales, we contend that the available evidence strongly supports our interpretation.

First, overpressures have been noted in the Wilcox Group and underlying units through several decades of drilling (e.g., Bebout et al., 1982; Burke et al., 2013). Second, the methods we used to estimate pore pressure are known to be applicable to the types of thick, continuously deposited Tertiary shale sections we studied. Other independent analyses we presented elsewhere (Kalinec et al., 2019; Zhu et al., 2019) also point to overpressures being present. The mud-weight data from neighboring wells indicate that drilling engineers have considered the shales to be overpressured. The splintery nature of cuttings in parts of the Wilcox to Midway shale interval adds further qualitative support to the presence of overpressures.

We conclude that the Tertiary and Upper Cretaceous shales of the Lower Wilcox Group, Midway, and Navarro are mildly to moderately overpressured, and anticipate that the actual pressure is somewhere between the pressure curves estimated using the density and sonic logs (Fig. 6).

Overpressures probably have a dual origin in the section of interest. First, the calculated sedimentation rates suggest that overpressures, associated with compaction disequilibrium, should have developed in the Midway and Navarro shales once they had been buried to a depth of approximately 1 km depth. Rapid loading by the overlying Wilcox Group and younger deposits should have further contributed to compaction disequilibrium.

Petrographically, there is abundant evidence for physical compaction, both of clay-rich rocks and sandstones and siltstones (Figs. 12 and 15). Inasmuch as compaction disequilibrium contributed to the development of overpressure in these rocks, we suggest that the amount of compaction at any given depth would have been greater had the shales been allowed to compact normally. Testing this hypothesis would require us to have samples from normally pressured rocks from the same stratigraphic interval. Following Day-Stirrat et al. (2008), it seems likely that part of the realignment of clay minerals is related to the transformation of smectite to illite, with the newly formed illite tending to be aligned nearly parallel to bedding and perpendicular to the contemporaneous maximum effective stress (i.e., vertical). This interpretation is

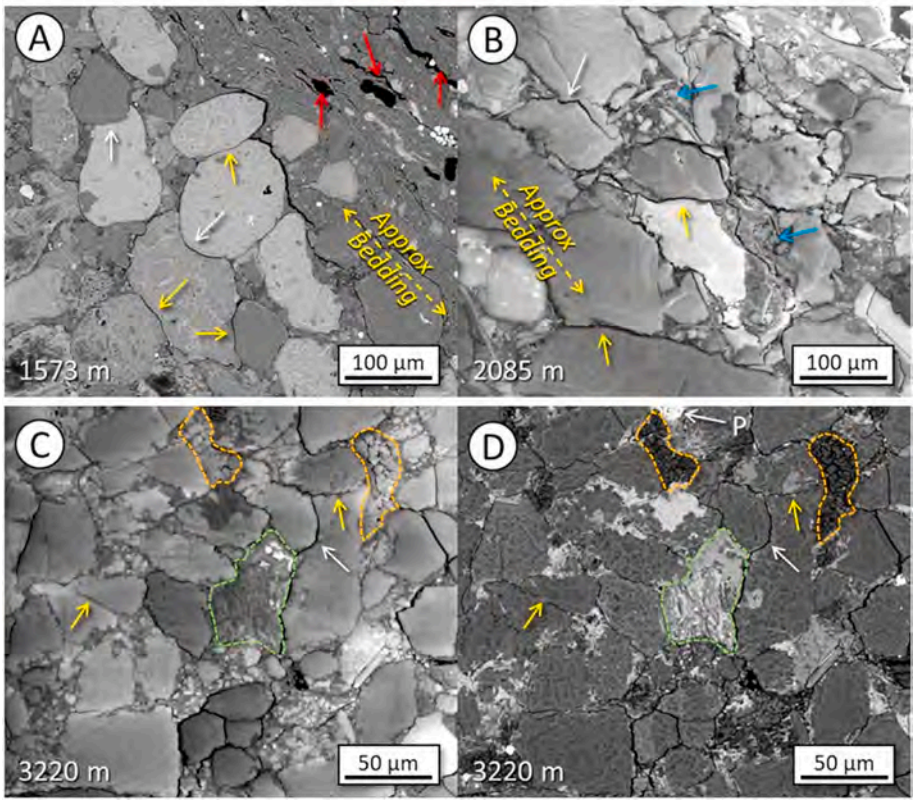

Fig. 12. SEM imagery of sandstones and siltstones included in the cuttings samples. The sandstones show evidence of compaction and diagenetic alteration/replacement of unstable minerals. A) Backscatter electron mode image of a sample from 1573 m. Concavo-convex (white arrows) and planar (yellow arrows) grain contacts between quartz grains indicate pressure solution. Organic matter (red arrows) in shale at upper right is particulate (Type III/IV). B) Secondary electron mode image of a sample from 2085 m. Yellow and white arrows as in Part A. Blue arrows point to clay-dominated areas that represent highly altered feldspars. C) and D) Secondary and backscatter electron mode images (respectively) of the same sample. Yellow and white arrows as in Part A. Areas outlined in orange are kaolinite. Area outlined in green represents highly altered feldspar. Dashed lines in Parts A and B indicate approximate orientation of bedding, as defined from low-magnitude imagery. Orientation of sample shown in Parts C and D could not be determined. (For interpretation of the references to color in this figure legend, the reader is referred to the Web version of this article.)

supported by our XRD data that shows a progressive increase in the amount of illite and chlorite, at the expense of smectite, with depth.

Given that we only have SEM images from one well, we choose not to speculate about how or if that type of imagery can be used to distinguish fabrics in normally compacting shales from shales experiencing compaction disequilibrium. In both cases, the shales should follow the same porosity-effective stress trend (Hart et al., 1995) and the effects of physical compaction should be similar. We would need to have SEM images from an area where the Wilcox Group and underlying shales are not overpressured, but with a similar burial history, to truly evaluate petrographic evidence for compaction disequilibrium.

A contribution to overpressures by clay-mineral diagenesis, primarily the smectite-to-illite transition, is a plausible supposition. Velocity and density data (Fig. 5) show a trend for the Lower Wilcox and Midway shales that is considered diagnostic of unloading. We note the presence of micro-quartz cement, probably associated with silica release during clay diagenesis, beginning in the Wilcox Group, and continuing down to the top of the Austin Chalk. The amount of smectite in mixed-layer clay decreases continuously from the surface down into the Wilcox Group and reaches an irreducible level in the Midway and Navarro shales. Although Thyberg et al. (2010) associated the growth of microquartz to the opal A – opal CT transition, the Upper Cretaceous and Tertiary siliciclastic deposits of our study would have lacked the significant contribution of biogenic silica (e.g., diatoms, radiolarians) present in their North Sea study area.

Given the low TOC, gas-prone nature of the organic matter, and relatively low thermal maturity in the section of interest (Fig. 6) we conclude that organic maturation is unlikely to have contributed to overpressure development. Studies of the Eagle Ford (e.g., Pommer and Milliken (2015; Osborne and Volk, 2020) and other source-rock reservoirs have documented the development of organic-matter-hosted nanopores as the thermal maturity (T_{max}) of the organic matter enters the gas window. Given that the oil-gas transition can be responsible for the development of significant overpressure via volume expansion (e.g., Meissner, 1976; Barker, 1990), we interpret the presence of oil, rather than nanoporous pyrobitumen, in the Wilcox Group, Midway Shale and Navarro Group as a petrographic indicator that in situ hydrocarbon maturation did not significantly contribute to overpressure development.

Jarvie (2012) noted several potential problems, e.g., dilution effects on T_{max} and TOC estimates, associated with use of cuttings for source-rock analyses. Although those challenges might affect quantitative prediction of source-rock yields, we contend that they will not materially affect the inferences we made based on *trends* in the data. Our ability to match the thermal maturity trends to borehole temperature trends strengthens our arguments that the former were not contaminated to an extent that makes them unsuitable for our purposes.

In light of these observations and analyses, we assert that the diagenetic products visible in the SEM images, and mineralogic transformations visible in the XRD data, are representative of shales in which a significant contribution to overpressure development comes from the transformation of smectite to illite and other clay minerals. We were unable to define petrographic characteristics at the nano-to micro-scale that could be used to identify compaction disequilibrium as an overpressure-generating mechanism.

5.2. *Shale microfabrics*

The term “shale” encompasses a wide variety of rock types (e.g., Potter et al., 2005; Lazar et al., 2015) and it is not appropriate to have a single conceptual model for their grain-scale fabric and the evolution thereof. This is especially if the definition of shales is based on wireline-log analyses such as using a volume-of-shale measure derived from a gamma-ray curve (e.g., Zhang, 2011), or even from more advanced petrophysical analyses. The nanometer-to centimeter-scale lithologic heterogeneity that is common in shales (e.g., Hart et al., 2013; Lazar et al., 2015, Figs. 11–16) is by its very nature below the resolution of the wireline logs used in pore-pressure prediction. Shales entirely

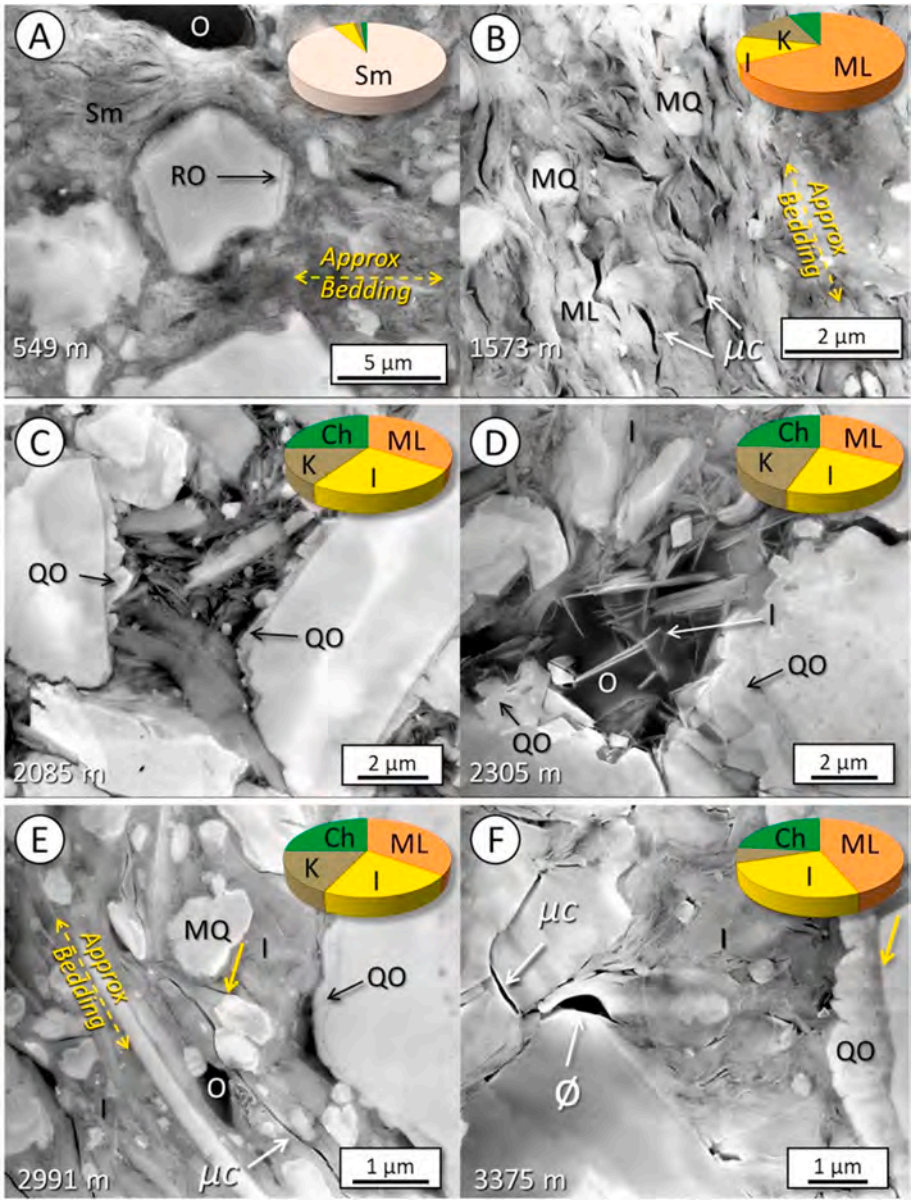

Fig. 13. Diagenetic quartz in shales. Pie charts in upper right show clay mineralogy of bulk cuttings sample (Sm-smectite; ML-mixed layer; I – illite/mica; K – kaolinite; Ch – chlorite). A) Sample from 549 m showing relict quartz overgrowths (RO) on a detrital quartz silt grain. Red arrow points to particulate organic matter. B) Sample from 1573 m showing diagenetic microquartz (MQ) within mixed-layer clays (ML). C) Sample from 2085 m. Angular to euhedral quartz overgrowths (yellow arrows) on quartz silt grains. D) Sample from 2305 m showing angular to euhedral quartz overgrowths on detrital silt. Pore space occupied by migrated oil (O) and diagenetic illite. Petrographic evidence indicates the oil migrated into the pores following precipitation of the illite. Solid pyrobitumen would not be expected given the low thermal maturity at this depth (Fig. 6). E) Sample from 2991 m showing diagenetic microquartz (MQ) and illite. Note the physical joining of illite to diagenetic quartz (yellow arrow suggesting the two minerals formed together. F) Sample from 3375 m showing quartz overgrowths on quartz silt (yellow arrow). Approximate bedding orientation (dashed) in Parts A, B and E defined by low-magnification view. Note the slot-shaped microcracks (µc) we interpret to be artifacts of sample recovery. All SEM images in this figure are secondary electron mode. (For interpretation of the references to color in this figure legend, the reader is referred to the Web version of this article.)

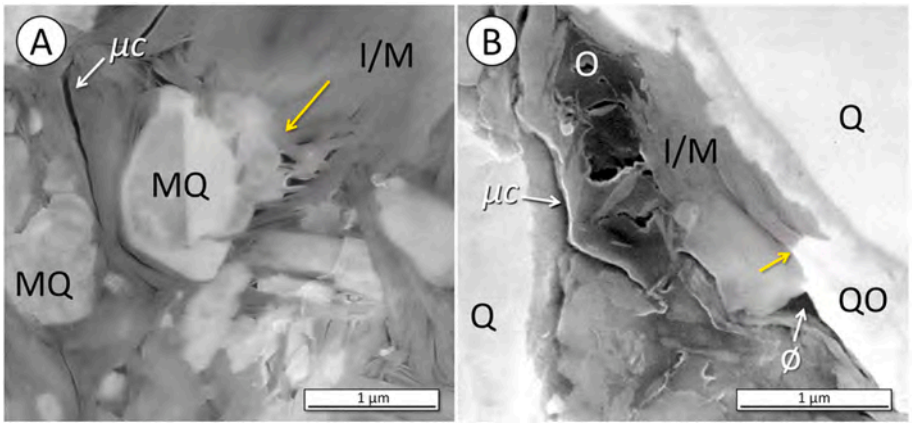

Fig. 14. Details of relationships between diagenetic quartz and diagenetic illite/mica as seen in secondary electron mode SEM imagery. (A) Microquartz (MQ) is physically attached to the illite/mica (I/M) at the yellow arrow, leaving nm-scale pores. (B) Quartz overgrowth (QO) is physically attached to I/M at the yellow arrow. Oil (O) is present in some of the pores but not all. In both cases, note the microcracks (µc) that are artifacts of sample retrieval. (For interpretation of the references to color in this figure legend, the reader is referred to the Web version of this article.)

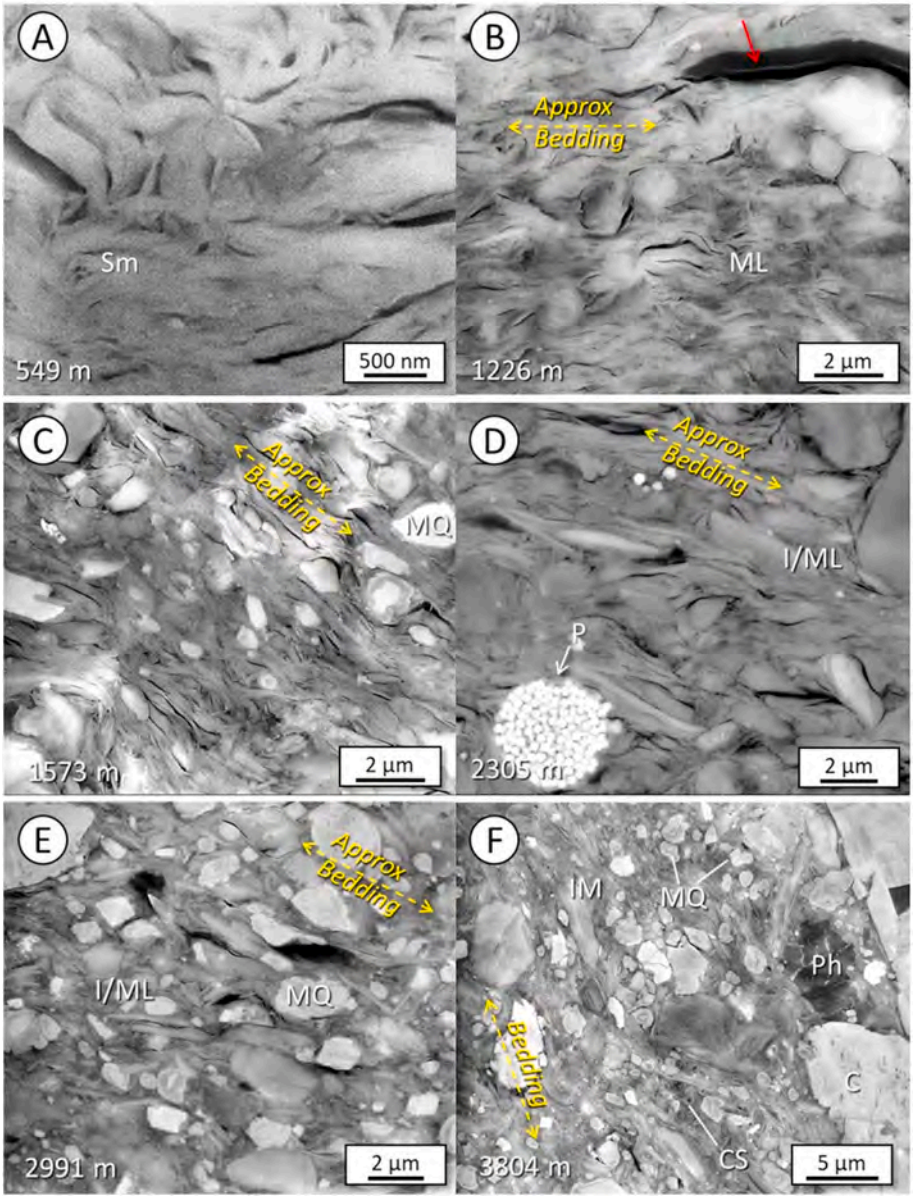

Fig. 15. SEM imagery of grain fabrics showing effects of mechanical and chemical compaction of clay minerals. Yellow arrows define approximate orientation of stratification as defined by low-magnification examination of individual cuttings samples (e.g., Fig. 11). (A) Detail of swelling smectite (Sm) from the shallowest sample. Hydrated cuttings from this level formed mud balls (Fig. 11A) and so the SEM imagery provides no useful information about the in-situ fabric of the clay minerals. (B) Grain alignment becomes evident by ~1200 m depth. Clays are predominantly mixed-layer smectite/illite. Red arrow points to compacted algal cyst. (C). Well-defined alignment of clay minerals is disrupted by sub-micron-scale crystals of diagenetic microquartz (MQ). XRD analyses show clays at this depth to be primarily illite-rich I/S and illite/mica. (D) Well-defined alignment of clay minerals (dominantly I/M) at 2305 m. Note pyrite framboid (Py) in lower left. (E) Although well compacted, abundant microquartz hinder the alignment of clays (mostly I/M) in this sample from 2991 m. (F) Calcite (C), phosphatic grains (Ph) and diagenetic quartz hinder the alignment of compacted clays (mostly I/M) from this Navarro Group shale sample. (CS – coccolith spine). All images collected using secondary electron mode, except for Part D which was collected in backscatter electron mode. (For interpretation of the references to color in this figure legend, the reader is referred to the Web version of this article.)

comprised of clay minerals (e.g., Fig. 18A) are geologically rare, although clay-dominated fabrics are traditionally assumed in most conceptual models of shale compaction (e.g., Moon, 1972; Sayers, 2005). The presence of rigid grains, e.g., quartz silt, hinders the realignment of clay minerals during burial (e.g., Curtis et al., 1980; Day-Stirrat et al., 2010) as seen in Figs. 16 and 18B. Fig. 16 also demonstrates that rigid diagenetic products such as microquartz and pyrite framboids can locally impede compaction. In clay-rich siltstones (Fig. 18C) that can be classified as shales from a grain-size and/or petrophysical perspective, compaction of clay minerals can be inhibited, and porosity loss is primarily through pressure solution (Fig. 12), physical deformation ("crushing"), or cementation.

The work of Landry et al. (2020a) was conducted in parallel to the study undertaken here with cuttings from Well 1. Those authors generated SEM mosaics, viewable at multiple scales, and used image analyses to quantify porosity. Porosity loss by compaction was complete in clay-dominated parts of the rock currently at ~2 km depth (i.e., Upper Wilcox). However, porosity could still be present a few microns away, in the same sample, if rigid detrital grains or cement locally prevented compaction as we show in Fig. 16. Examples of those mosaics are presented by Landry et al. (2020b). Those findings, ours, and others (e.g., Hart et al., 2013), highlight the need to examine shales at multiple scales before applying simple conceptual models to thick shale sections.

Local porosity preservation by rigid grains (Schieber, 2010) could be considered a type of "irreducible porosity", providing an explanation for the presence of shale porosity at substantial burial depth (as deep as 6500 m; Schicker et al., 2021) that is not due to bound water in smectite layers (e.g., Lahann and Swarbrick, 2011). A combination of SEM imaging and XRD analyses, such as employed here, could help define the extent to which either of these pore types is present.

The nano-scale pore throats associated with clays that are locally sheltered from physical compaction (Fig. 16) are likely to be the "connecting pores" inferred to be present in some shales (Bowers and Katsube, 2002). The microcracks we observe in some images are also potential candidates, but the origin of microcracks in SEM imagery of shales has been the source of rich debate (e.g., Loucks et al., 2012), and our observations support the concept that the great majority (if not all) of these are artifacts due to pressure release, mechanical stresses during drilling, and dehydration. We suggest that the multi-scale examination of shale samples (from cuttings, core, or outcrop), such as shown in

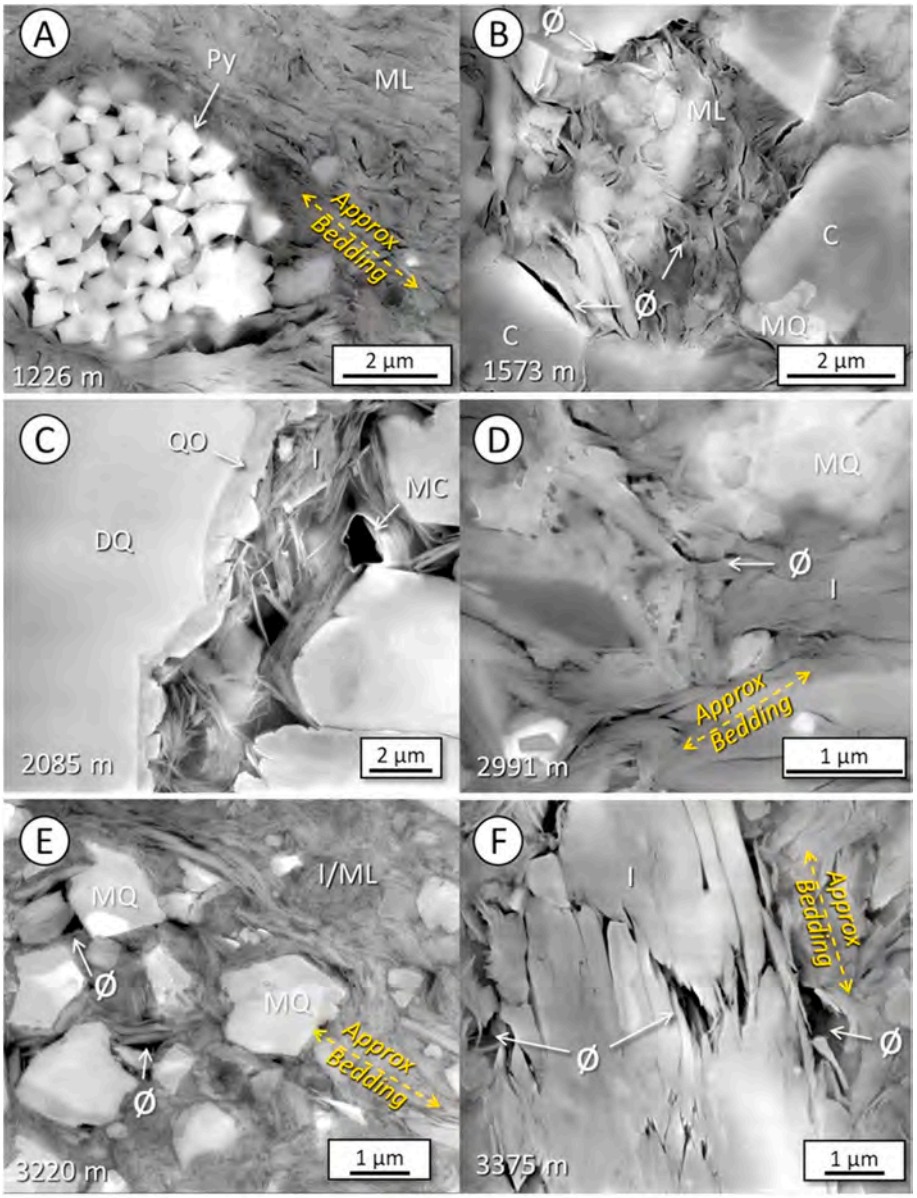

Fig. 16. SEM imagery of pores that are preserved despite compaction. (A) Porosity in pyrite framboid. (B) Micron-scale areas between larger, rigid grains (calcite cement in a siltstone – C) form areas where clay minerals were not subjected to physical compaction. Note the random alignment of mixed-layer clays (ML) in the center of the image that preserves nano-scale pores. (C) Random alignment of illite within an area sheltered from compaction by detrital quartz grains (DQ) and quartz overgrowths (QO). Oil has partly filled the void between quartz grains, forming a meniscus contact (MC) in this Upper Wilcox siltstone. Oil migration followed precipitation of the illite. Solid pyrobitumen would not be expected given the low thermal maturity at this depth (Fig. 6). (D) Nano-pores preserved at junctions between diagenetic illite crystals that grew at different orientations. (E) The growth of microquartz created pressure shadows where nanoporosity could be preserved. Note bending of clays around some of the rigid microquartz crystals. (F) The larger (detrital?) illite in the center of the image preserved intra-particle pores where it was ruptured and outside where it is in contact with other clays. All images collected using secondary electron mode.

Fig. 17, should be an integral part of any study investigating the origins of microcracks.

5.3. Utility of cuttings

In a perfect world, shale compaction would be studied via whole cores that would enable samples to be oriented for SEM analyses. Core samples can be linked to precise depths, whereas cuttings represent an interval (~3 m in our case) and contamination from shallower levels is a known problem. Core samples also give the option to collect actual porosity and permeability data on the plugs. In the real world, the cost of coring through shale intervals several km thick is prohibitive, except perhaps for some specific research contexts.

Cuttings are a cheap and abundant source of rock for various types of analyses. Despite the drawbacks we mention above, analysis of cuttings can provide significant qualitative insights into the diagenetic and burial history of the geological section when integrated with other data types. As we show herein, the cuttings exhibit the expected progressive increase in grain alignment, decrease in porosity, and increased crystallinity with depth. This type of information provides valuable data to resolve that the major factor driving overpressure in this section is a combination of compaction and compaction/diagenesis (smectite/illite transition). Analysis of mineral and clay types in the cuttings also provides key petrological information as to what constitutes a "shale" when filtering data for use in pore pressure analysis.

6. Conclusions

We integrated cuttings analyses, wireline logs and other data types to investigate the origins of overpressures in a succession of Upper Cretaceous and Tertiary shales nearly 4 km thick. We chose to integrate tools and techniques from the study of source-rock ("shale") reservoirs with the types of wireline log analyses used for pore-pressure prediction. Our experiment was designed to provide information about overpressures, but also to provide insights about the utility of our approach for that purpose.

We used standard, wireline-log-based tools for pore-pressure estimation. Their use is warranted, given the geologic context of our study area. We infer that the section is normally pressured down to ~2.5 km depth (middle portion of the Wilcox Group) and that overpressures

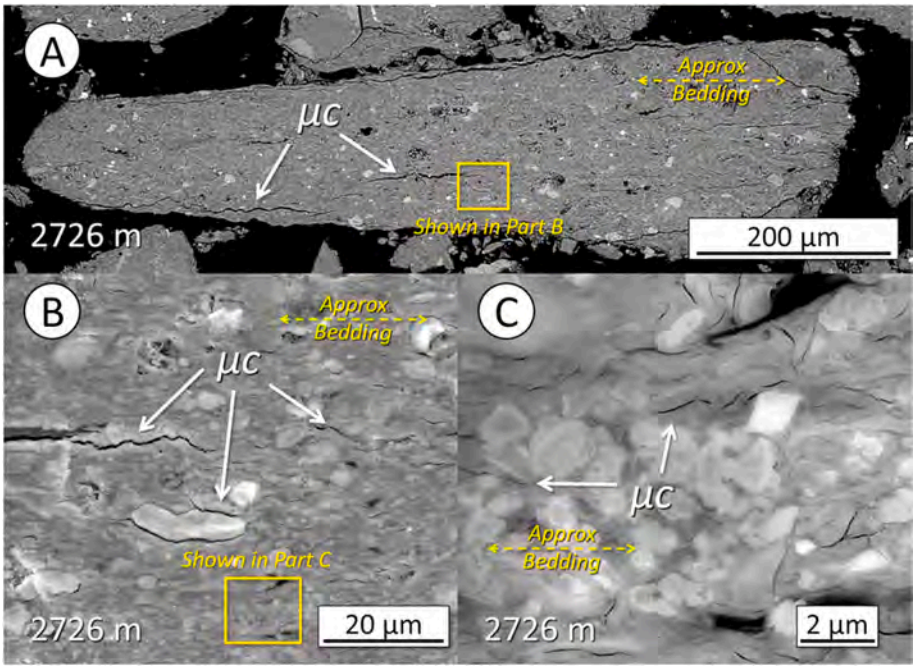

Fig. 17. These images show micro-cracks (μc) at three different magnifications in a single shale chip. In this case, the microcracks are demonstrably artifacts. At low magnification (A) the elongate shape of the chip is approximately parallel to cracks that can be interpreted as being artifacts formed by pressure release as cuttings are brought to the surface. Microcracks of similar orientation but smaller size are visible at higher magnifications (B, C). We interpret all microcracks in these images to be artifacts. Part A collected using backscatter electron mode and Parts B and C collected using secondary electron mode.

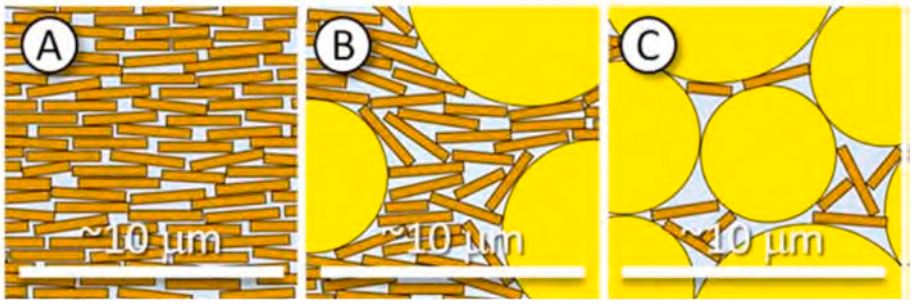

Fig. 18. Shale texture, i.e., the mix of grain sizes present, affects porosity preservation. A) A common assumption for shale texture/porosity is that clays (brown) realign with bedding and destroy porosity during compaction. B) Many shales consist of matrix-supported textures where sand/silt grains "float" in a clay matrix. Clay plates are not free to fully align in this case, and porosity within clay fabrics can partially be preserved. C) In silt-rich shales, silt grains form a rigid framework and interstitial clays do not become aligned due to effective-stress orientation. In all cases, both the rigid grains ("silt") and clays can be either diagenetic or detrital in origin. (For interpretation of the references to color in this figure legend, the reader is referred to the Web version of this article.)

subsequently increase with depth, eventually becoming moderate in the section above the Eagle Ford producing interval. We chose not to include the Eagle Ford in our analyses because of that unit's differing mineralogic composition and much higher organic content.

When integrated, the cuttings-based XRD, Rock-Eval, and SEM analyses provide direct indication of the compaction and diagenetic processes taking place in the development of the overpressure defined by the wireline logs and mud weights. Clear indications of the smectite to illite transition, seen in both the XRD and SEM data, coincide with the onset of "unloading" as seen in the wireline-log data and the increase in pore pressure from the Lower Wilcox downward into the Midway shale. The mineralogic transition defined by XRD also corresponds to the appearance of diagenetic quartz, as both "microquartz" and overgrowths, in the shales. The silica for that cement was released during the smectite to illite conversion, hence its presence in overpressured shales is an indicator that some of the excess pore pressure may have developed because of clay diagenesis.

The SEM data document several ways in which porosity can be preserved in the deeper overpressured shales. As such, the porosity "floor" typically defined by wireline log analyses of shales is not necessarily tied to only bound water in the clays. Primary porosity can be preserved to great depth by shale microfabrics wherein compaction is prevented the shielding effects of silt grains or rigid cements (e.g., pyrite, quartz) in the clay matrix. This knowledge of retained primary porosity can be important when designing "normal" compaction curves to interpret pore pressure.

Integrating the cuttings observations and evaluations also provides important information for the understanding of the pressure generation history of the basin. Detailed knowledge of where the smectite/illite transformation begins in the section can provide information as to how much uplift may have taken place, or whether the onset of overpressure is an "unloading event" or from some other source. Rock-Eval data acquired over the course of cuttings samples can indicate how much, if any of the modeled and/or observed pore pressure is derived from HC maturation and provide a more detailed snapshot of the current state of maturation in the entire section in the basin. Despite the limitations discussed above, the integration of cuttings data provides a relatively inexpensive way to incorporate "real" data into the pressure and maturation history of a basin.

Declaration of competing interest

The authors declare that they have no known competing financial interests or personal relationships that could have appeared to influence the work reported in this paper.

Data availability

The authors do not have permission to share data.

Acknowledgments

Funding for this research was supplied by Equinor. We thank Andy Aplin, an anonymous reviewer, and Editor-in-Chief Qinhong Hu for their efforts to improve the manuscript. Responsibility of any remaining errors or omissions are ours.

References

Aplin, A.C., Matenaar, I.F., McCarty, D.K., van der Pluijm, B.A., 2006. Influence of mechanical compaction and clay mineral diagenesis on the microfabric and pore-scale properties of deep-water Gulf of Mexico mudstones. Clay Clay Miner. 54 (4), 500–514. https://doi.org/10.1346/CCMN.2006.0540411.

Aplin, A.C., Macquaker, J.H.S., 2011. Mudstone diversity: origin and implications for source, seal, and reservoir properties in petroleum systems. AAPG (Am. Assoc. Pet. Geol.) Bull. 95, 2031–2059.

Avseth, P., Mukerji, T., Mavko, G., 2010. Quantitative Seismic Interpretation: Applying Rock Physics Tools to Reduce Interpretation Risk. Cambridge University Press, Cambridge, p. 359.

Barker, C., 1990. Calculated volume and pressure changes during the thermal cracking of oil to gas in reservoirs. AAPG (Am. Assoc. Pet. Geol.) Bull. 74, 1254–1261.

Beaumont, E.A., Fiedler, F., 1999. Formation fluid pressure and its application. In: Beaumont, E.A., Foster, N.H. (Eds.), AAPG Treatise of Petroleum Geology/Handbook of Petroleum Geology: Exploring for Oil and Gas Traps, pp. 5-1–5-64.

Bebout, D.G., Weise, B.R., Gregory, A.R., Edwards, M.B., 1982. Wilcox Sandstone Reservoirs in the Deep Subsurface along the Texas Gulf Coast; Their Potential for Production of Geopressured Geothermal Energy, vol. 117. University of Texas at Austin, Bureau of Economic Geology Report of Investigations No, p. 125.

Boles, J.R., Franks, S.G., 1979. Clay diagenesis in Wilcox sandstones of southwest Texas: implications of smectite diagenesis on sandstone cementation. J. Sediment. Petrol. 49, 55–70.

Bodner, D.P., Sharp Jr., J.M., 1988. Temperature variations in south Texas subsurface. AAPG (Am. Assoc. Pet. Geol.) Bull. 72, 21–37.

Bowers, G.L., 1995. Pore pressure estimation from velocity data: accounting for overpressure mechanisms besides undercompaction. SPE Drill. Complet. 10 (2), 89–95. https://doi.org/10.2118/27488-PA.

Bowers, G.L., 2001. Determining an appropriate pore-pressure estimation strategy. Offshore Techn. Conf. OTC 13042, 14p. https://doi.org/10.4043/13042-MS.

Bowers, G., Katsube, T., 2002. The role of shale pore structure on the sensitivity of wireline logs to overpressure. In: Huffmann, A.R., G L, B. (Eds.), Pressure Regimes in Sedimentary Basins and Their Prediction, vol. 76. AAPG Memoir, pp. 43–60.

Burke, L.A., Kinney, S.A., Dubiel, R.F., Pitman, J.K., 2013. Regional Maps of Subsurface Geopressure Gradients of the Onshore and Offshore Gulf of Mexico Basin. USGS Open-File. Report 2013-1058, 3 sheets.

Carpenter, C., 2015. Eagle Ford Shale well control: drilling and tripping. J. Petrol. Technol. 104–108.

Cather, S.M., Chapin, C.E., Kelley, S.A., 2012. Diachronous episodes of Cenozoic erosion in southwestern North America and their relationship to surface uplift, paleoclimate, paleodrainage, and paleoaltimetry. Geosphere 8, 1177–1206.

Curtis, C.D., Lipshie, S.R., Oertel, G., Pearson, M.J., 1980. Clay orientation in some Upper Carboniferous mudrocks, its relationship to quartz content and some inferences about fissility, porosity and compactional history. Sedimentology 27, 333–339.

Day-Stirrat, R.J., Aplin, A.C., Środoń, J., van der Pluijm, B.A., 2008. Diagenetic reorientation of phyllosilicate minerals in paleogene mudstones of the podhale basin, southern Poland. Clay Clay Miner. 56 (1), 100–111. https://doi.org/10.1346/CCMN.2008.0560109.

Day-Stirrat, R.J., Dutton, S.P., Milliken, K.L., Loucks, R.G., Aplin, A.C., Hillier, S., van der Pluijm, B.A., 2010. Fabric anisotropy induced by primary depositional variations in the silt: clay ratio in two fine-grained slope fan complexes: Texas Gulf Coast and northern North Sea. Sediment. Geol. 226 (1–4), 42–53. https://doi.org/10.1016/j.sedgeo.2010.02.007.

Day-Stirrat, R.J., Flemings, P.B., You, Y., Aplin, A.C., van der Pluijm, B.A., 2012. The fabric of consolidation in Gulf of Mexico mudstones. Mar. Geol. 295–298, 77–85.

Denne, R., Breyer, J., Callender, A., Hinote, R., Kariminia, M., Kosanke, T., Kita, Z., Lees, J., Rowe, H., Spaw, J., Tur, N., 2016. Biostratigraphic and geochemical constraints on the stratigraphy and depositional environments of the Eagle Ford and Woodbine Groups of Texas. In: Breyer, J.A. (Ed.), The Eagle Ford Shale: A Renaissance in U.S. Oil Production: AAPG Memoir 110, pp. 1–86.

Dutta, N.C., 2016. Effect of chemical diagenesis on pore pressure in argillaceous sediment. Lead. Edge 35, 523–527. https://doi.org/10.1190/tle35060523.1.

Eaton, B.A., 1975. The Equation for Geopressure Prediction from Well Logs. Fall Meeting of the Society of Petroleum Engineers of AIME: Society of Petroleum Engineers. https://doi.org/10.2118/5544-MS.

Fertl, W.H., 1976. Drilling data detect and evaluate abnormal formation pressures. In: Fertl, Walter H., Chilingarian, George V., Rieke, Herman H. (Eds.), Abnormal Formation Pressures: Implications to Exploration, Drilling, and Production of Oil and Gas Resources, Developments in Petroleum Science, vol. 2, pp. 117–175.

Galloway, W.E., 2008. Depositional evolution of the Gulf of Mexico sedimentary basin. In: Miall, A.D. (Ed.), The Sedimentary Basins of the United States and Canada: The Netherlands. Elsevier, pp. 505–549.

Gordon, D.S., Flemings, P.B., 1998. Generation of overpressure and compaction-driven fluid flow in a Plio-Pleistocene growth-faulted basin. Eugene Island 330, offshore Louisiana: Basin Res. 10, 177–196.

Hart, B.S., Flemings, P.B., Deshpande, A., 1995. Porosity and pressure: role of compaction disequilibrium in the development of geopressures in a Gulf Coast Pleistocene basin. Geology 23, 45–48.

Hart, B.S., Godet, A., Pope, M.C., Griffith, C., 2020. Geologic Controls on Production: Eagle Ford and Austin Chalk. SEPM Field Guidebook (in press).

Hart, B., Macquaker, J., Taylor, K., 2013. Mudstone ("shale") depositional and diagenetic processes: implications for seismic analyses of source-rock reservoirs. Interpretation 1, B7–B26.

Hermanrud, C., Wensaas, L., Teige, G.M.G., Vik, E., Bolas, H.M.N., Hansen, S., 1998. Shale porosities from well logs on Haltenbanken (offshore mid-Norway) show no influence of overpressuring. In: Law, Be, Ulmishek, G.F., Slavin, V.I. (Eds.), Abnormal Pressures in Hydrocarbon Environments, vol. 70. AAPG Bulletin, pp. 65–85.

Hower, J., Eslinger, E.V., Hower, M.E., Perry, E.A., 1976. Mechanism of burial metamorphism of argillaceous sediment. Geol. Soc. Am. Bull. 87, 725–737.

Issler, D.R., 1992. A new approach to shale compaction and stratigraphic restoration. Beaufort-MacKenzie basin and MacKenzie Corridor, northern Canada: AAPG (Am. Assoc. Pet. Geol.) Bull. 76, 289–300.

Jarvie, D.M., 2012. Shale resource systems for oil and gas: Part 1—shale-gas resource systems. In: Breyer, J.A. (Ed.), Shale Reservoirs—Giant Resources for the 21st Century: AAPG Memoir 97, pp. 69–87.

Jennings, S., Thompson, G., 1986. Diagenesis of plio-pleistocene sediments of the Colorado river delta, southern California. J. Sediment. Res. 56, 89–98.

Kalinec, J., Hart, B.S., 2021. Reservoir pressure mapping from well-test data: an Eagle Ford example. GeoGulf Transactions 71, 149–155.

Kalinec, J., Paryani, M., Ouenes, A., 2019. Estimation of 3D distribution of pore pressure from surface drilling data – application to optimal drilling and frac hit prevention in the Eagle Ford. URTEC 511, 12.

Lahann, R.W., 2002. Impact of smectite diagenesis on compaction modeling and compaction equilibrium. In: Huffman, A., Bowers, G. (Eds.), Pressure Regimes in Sedimentary Basins, vol. 76. AAPG Memoir, pp. 61–72.

Lahann, R.W., Swarbrick, R.E., 2011. Overpressure generation by load transfer following shale framework weakening due to smectite diagenesis. Geofluids 11, 362–375. https://doi.org/10.1111/j.1468-8123.2011.00350.x.

Landry, C.J., Hart, B.S., Prodanovic, M., 2020a. Comparison of wireline log and SEM image-based measurements of porosity in overburden shales. URTeC 3141, 16.

Landry, C., Prodanovic, M., Hart, B., 2020b. High-resolution SEM image mosaics of overburden shales: Wilcox Group, Midway, Navarro. Digital Rocks Portal. http://www.digitalrocksportal.org/projects/310.

Lazar, O.R., Bohacs, K.M., Macquaker, J.H.S., Schieber, J., Demko, T.M., 2015. Capturing key attributes of fine-grained sedimentary rocks in outcrops, cores, and thin sections: nomenclature and description guidelines. J. Sediment. Res. 85, 230–246.

Loucks, R.G., Reed, R.M., Ruppel, S.C., Hammes, U., 2012. Spectrum of pore types and networks in mudrocks and a descriptive classification for matrix-related mudrock pores. AAPG (Am. Assoc. Pet. Geol.) Bull. 96, 1071–1098. https://doi.org/10.1306/08171111061.

Mace, R.E., Smyth, R.C., Xu, L., Liang, J., 2000. Transmissivity, Hydraulic Conductivity, and Storativity of the Carrizo-Wilcox Aquifer in Texas. Texas Bureau of Economic Geology Technical Report, p. 76. http://www.twdb.texas.gov/publications/reports/contracted_reports/doc/99483279_CzWx_hydroproperties.pdf. (Accessed 20 January 2020). accessed.

Meissner, F.F., 1976. Petroleum Geology of the Bakken Formation Williston Basin, North Dakota and Montana, (24th Annual Conference, Williston Basin Symposium) Montana. Geological Society, pp. 207–227.

Mitchell, C., 2017. Characterization of the Cretaceous "Olmos" Formation in the Somerset Oilfield, South Texas. AAPG Search & Discovery Article 20411. (Accessed 14 December 2019). Accessed.

Moon, C.F., 1972. The microstructures of clay sediments. Earth Sci. Rev. 8, 303–321.

Morris, S., Vestal, B., O'Neill, K., Moretti, M., Franco, C., Hitchings, N., Zhang, J., Grace, J., 2015. The pore pressure regime of the northern Gulf of Mexico: geostatistical estimation and regional controls. AAPG (Am. Assoc. Pet. Geol.) Bull. 99, 91–118. https://doi.org/10.1306/07221413148.

Nagihara, S., Smith, M.A., 2008. Regional overview of deep sedimentary thermal gradients of the geopressured zone of the Texas–Louisiana continental shelf. AAPG (Am. Assoc. Pet. Geol.) Bull. 92, 1–14.

Olariu, M.I., Zeng, H., 2018. Prograding muddy shelves in the paleogene Wilcox deltas, south Texas Gulf coast. Mar. Petrol. Geol. 91, 71–88.

Osborne, M., Volk, H., 2020. Understanding variations in reservoir porosity in the Eagle Ford Shale using scanning electron microscopy: implications for basin modelling. In: Dowey, P., Osborne, M., Volk, H. (Eds.), Application of Analytical Techniques to Petroleum Systems, vol. 484. Geological Society, London, Special Publication, pp. 229–239.

Perry, E., Hower, J., 1972. Late-stage dehydration in deeply buried pelitic Sediments. AAPG (Am. Assoc. Pet. Geol.) Bull. 56 (10), 2013–2021.

Pommer, M., Milliken, K., 2015. Pore types and pore size distributions across thermal maturity, Eagle Ford Formation, southern Texas. AAPG (Am. Assoc. Pet. Geol.) Bull. 99, 1713–1744.

Potter, P.E., Maynard, J.B., Depetris, P.J., 2005. Mud and Mudstones: Introduction and Overview. Springer, Berlin, p. 297.

Sayers, C.M., 2005. Seismic anisotropy of shales. Geophys. Prospect. 53, 667–676.

Schieber, J., 2010. Common Themes in the Formation and Preservation of Intrinsic Porosity in Shales and Mudstones—Illustrated with Examples across the Phanerozoic: N. 132370-MS. SPE Unconventional Gas Conference, Pittsburgh, Pennsylvania, USA. February 23–25, 2010.

Schieber, J., 2013. SEM observations on Ion-milled samples of Devonian Black Shales from Indiana and New York: the petrographic context of multiple pore types. In: Camp, W., Diaz, E., Wawak, B. (Eds.), Electron Microscopy of Shale Hydrocarbon Reservoirs: AAPG Memoir 102, pp. 153–172.

Schieber, J., Lazar, R., Bohacs, K., Klimentidis, B., Dumitrescu, M., Ottmann, J., 2016. An SEM study of porosity in the Eagle Ford Shale of Texas— pore types and porosity distribution in a depositional and sequence stratigraphic context. In: Breyer, J.A. (Ed.), The Eagle Ford Shale: A Renaissance in U.S. Oil Production: AAPG Memoir 110, pp. 167–186.

Swarbrick, R., 2012. Review of pore-pressure prediction challenges in high-temperature areas. Lead. Edge 31, 1288–1294. https://doi.org/10.1190/tle31111288.1.

Swarbrick, R.E., Osborne, M.J., 1998. Mechanisms that generate abnormal pressures: an overview. In: Law, B.E., Ulmishek, G.F., Slavin, U.I. (Eds.), Abnormal Pressures in Hydrocarbon Environments: AAPG Memoir 70: AAPG Special Volumes, pp. 13–34.

Thyberg, B., Jahren, J., Winje, T., Bjørlykke, K., Faleide, J.I., Marcussen, Ø., 2010. Quartz cementation in Late Cretaceous mudstones, northern North Sea: changes in rock properties due to dissolution of smectite and precipitation of micro-quartz crystals. Mar. Petrol. Geol. 27 (8), 1752–1764. https://doi.org/10.1016/j.marpetgeo.2009.07.005.

Tingay, M.R.P., Hillis, R.R., Swarbrick, R.E., Morley, C.K., Damit, A.R., 2009. Origin of overpressure and pore-pressure prediction in the Baram province, Brunei. AAPG (Am. Assoc. Pet. Geol.) Bull. 93, 51–74.

Worden, R.H., Morad, S., 2003. Clay minerals in sandstones: controls on formation, distribution and evolution. In: Worden, R.H., Morad, S. (Eds.), Clay Mineral Cements in Sandstones. Blackwell Publishing Ltd., Oxford, UK, pp. 1–41.

Xia, X., Michael, G.E., Gao, Y., 2020. Preservation of lateral pressure disequilibrium during the uplift of shale reservoirs. AAPG (Am. Assoc. Pet. Geol.) Bull. 104, 825–843.

Zhang, J., 2011. Pore pressure prediction from well logs: methods, modifications, and new approaches. Earth Sci. Rev. 108, 50–63.

Zhu, Y., Hart, B.S., Ebrom, D., Kalinec, J., Wensaas, L., 2019. Evolutionary Rock Physics for Mudrock Pressure Modeling. SEG Technical Program Expanded Abstracts, p. 4, 2019.